Application of structural symmetries in the plane-wave-based transfer-matrix method for three-dimensional photonic crystal waveguides

Zhi-Yuan Li* and Kai-Ming Ho
Ames Laboratory and Department of Physics and Astronomy, Iowa State University, Ames, Iowa 50011, USA
(Received 11 July 2003; revised 2 October 2003; published 29 December 2003)

The plane-wave-based transfer-matrix method (TMM) exhibits a peculiar advantage of being capable of solving eigenmodes involved in an infinite photonic crystal and electromagnetic (EM) wave propagation in finite photonic crystal slabs or even semi-infinite photonic crystal structures within the same theoretical framework. In addition, this theoretical approach can achieve much improved numerical convergency in solution of photonic band structures than the conventional plane-wave expansion method. In this paper we employ this TMM in combination with a supercell technique to handle two important kinds of three-dimensional (3D) photonic crystal waveguide structures. The first one is waveguides created in a 3D layer-by-layer photonic crystal that possesses a complete band gap, the other more popular one is waveguides built in a two-dimensional photonic crystal slab. These waveguides usually have mirror-reflection symmetries in one or two directions perpendicular to their axis. We have taken advantage of these structural symmetries to reduce the numerical burden of the TMM solution of the guided modes. The solution to the EM problems under these mirror-reflection symmetries in both the real space and the plane-wave space is discussed in a systematic way and in great detail. Both the periodic boundary condition and the absorbing boundary condition are employed to investigate structures with or without complete 3D optical confinement. The fact that the EM field components investigated in the TMM are collinear with the symmetric axes of the waveguide brings great convenience and clarity in exploring the eigenmode symmetry in both the real space and the plane-wave space. The classification of symmetry involved in the guided modes can help people to better understand the coupling of the photonic crystal waveguides with external channels such as dielectric slab or wire waveguides.

DOI: 10.1103/PhysRevB.68.245117 PACS number(s): 42.70.Qs, 42.50.Dv, 32.80.−t

I. INTRODUCTION

In recent years photonic crystals (PC's), a class of artificial materials made up of periodic dielectric or metallic building blocks, have attracted extensive interest due to their powerful capability to control and manipulate the propagation of electromagnetic (EM) waves. This power is brought about by the existence of a photonic band gap (PBG), which is a range of frequencies within which EM waves cannot propagate.[1,2] Line defects introduced into an otherwise perfect PC can serve as an efficient channel for guiding light, and may become an important type of composite functional element in future ultrasmall photonic integrated circuits that are built on the photonic crystal platform. It has been shown that efficient confinement and propagation of EM waves through these PC waveguide channels can be achieved at frequencies within the PBG.[3,4] In principle, the efficient guiding functionality strongly requests a three-dimensional (3D) photonic crystal that exhibits a complete band gap. One of the examples is the layer-by-layer photonic crystal that was first proposed by Ho and co-workers and has been under extensive studies since.[5–12] This structure is made from stacks of dielectric rods in a woodpile fashion. A waveguide can form by simply removing a rod from this photonic crystal. Although promising progress has been made towards constructing a workable photonic crystal sample at the fundamental optic-communication wavelength of 1.55 μm,[6–8] it still remains a challenge to bring functional elements such as a waveguide into this tiny platform. Therefore, most experimental works are limited in the microwave regime.[10,12] As a comparison, waveguides created in a two-dimensional (2D) photonic crystal slab are much easier to realize experimentally in the near-infrared regime by means of current advanced lithographic techniques.[13–18] For this reason, these 2D PC slab waveguides have become the most popular systems under study in these days. The optical confinement in these 2D PC slab waveguides relies on the 2D band gap in the lateral plane and index-guiding mechanism in the vertical direction of the slab.

Theoretical understanding of EM wave propagation within a PC waveguide can play an important role in designing and constructing an optical integrated circuit built on the photonic crystal platform. To accomplish this task, people usually adopt a plane-wave expansion method (PWM) (Refs. 19–21) to envision the localized eigenmodes (guided modes) supported by the waveguide,[9,11,13] and a finite-difference time-domain (FDTD) approach[22] to observe the dynamics of EM waves propagating in the waveguide and the corresponding transmission and reflection spectra.[3,4,9,14–18] The FDTD technique can also be employed to find out the guided modes.[9,14] As this method can handle both periodic and aperiodic structures, it has been dominantly used to understand the optical properties of straight waveguide, waveguide bends, and waveguide coupling with cavities.[3,4,9,14–18] Yet, it has been well-known that the FDTD technique can face with severe difficulty and inconvenience when it is employed to extract very fine quantitative information about the transmission and reflection spectra for an functional element placed in the background of a photonic crystal, which is an inhomogeneous medium. This situation can be found in solution of the transmission efficiency through a sharp 3D waveguide

bend, where fine and reliable spectra will impose too much numerical burden, or even becomes intractable.[3,9,14]

Another popular numerical approach, the transfer-matrix method (TMM),[23–30] is also widely used in the photonic crystal community. A TMM can be classified into the real-space TMM[23] and plane-wave-based TMM,[24–30] depending on what basis function is used to represent the EM fields. This approach can place the solution of the photonic band structures for a periodic photonic crystal and the scattering problem of a finite PC slab within the same theoretical framework. When it is combined with a supercell technique, the TMM can also handle wave propagation in a PC waveguide. For a straight waveguide, the numerical burden involved in the TMM simulation is logarithmatically proportional to the waveguide length, a big relief compared to the linear dependence associated with the FDTD technique. This advantage is in part due to the periodicity of the PC waveguide and in part due to the efficient layer-doubling recursion algorithm existing in the mathematical structure of the TMM.[23,24,33] In addition, the TMM is working in the frequency domain, and therefore is most suitable for accurate solution of the spectra. Finally, this approach can be successfully expanded to handle wave propagation in semi-infinite photonic crystal and related waveguide structures,[30] and therefore can efficiently explore the optical properties of a variety of functional elements embedded into the photonic crystal background. For these reasons, it is worthwhile to go deeper into this powerful theoretical tool.

Even if the TMM is armed with these merits and powers, numerical simulations for a 3D PC waveguide structure under the usage of a sufficiently large supercell still require extensive computer memory space and are quite time consuming in order to achieve high enough calculation accuracy. For instance, in the plane-wave-based TMM, the required storage space is parabolically proportional to the number of plane waves adopted to expand the EM fields in the cross-sectional plane of the waveguide. Therefore, it is highly desirable to find out some ways to release this memory-space requirement and reduce computational time. Various lattice symmetries such as translational and rotational symmetries existing in a photonic crystal system have been exploited to reduce the computational burden of the TMM.[27,29,31–33] This observation suggests that we should take a closer look at the 3D PC waveguides and try to find out the structural symmetries that might lie behind them. Since a 3D PC waveguide is essentially a quasi-1D structure, the possible number of structural symmetry is greatly limited compared to those that can be found in a 3D photonic crystal. Actually, mirror-reflection symmetries along one or two directions in the cross-sectional plane of the waveguide are the only ones that can be found in the abovementioned 3D layer-by-layer PC waveguides and 2D PC slab waveguides. This can be seen when one looks at the schematic configuration of these two types of 3D PC waveguide in Figs. 1 and 7, respectively. In addition to the reduction in numerical computation, the usage of structural symmetry can also help to reveal the symmetry of fields involved in the guided mode. This mode-symmetry knowledge will play an important role in understanding the coupling of the PC waveguides with external waveguide channels, such as dielectric slab or wire waveguides.[30,34,35] These conventional waveguides also possess structural symmetries that might be same as the PC waveguides.

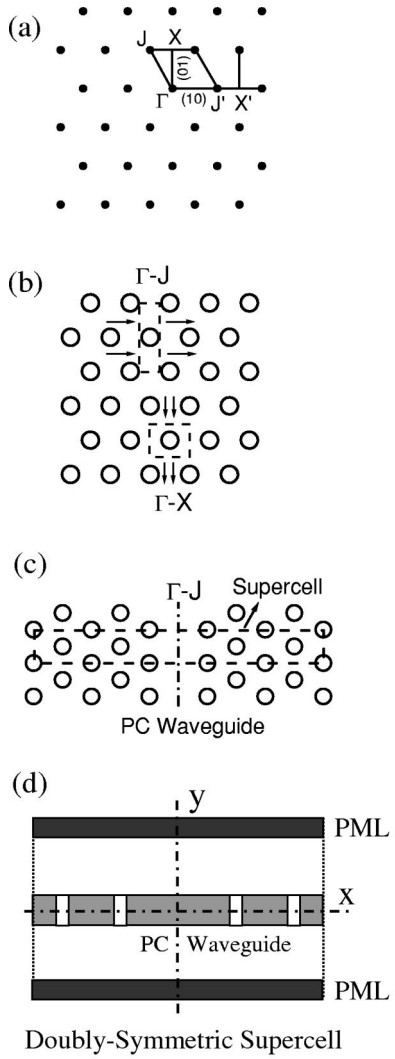

FIG. 1. Schematic configuration and symmetry in 2D PC slab and slab waveguide structures. (a) Brillouin zone and high symmetric points for a triangular lattice. (b) Symmetric unit cells used in solution of band diagrams for a 2D PC slab along the ΓJ and ΓX directions. (c) Top view of the symmetric supercell used in solution of the band diagrams of guided modes in a PC slab waveguide. (d) Side view of the supercell for the slab waveguide. The PML's at the boundary of the supercell are not indispensable.

In this paper, we will systematically investigate the TMM under the mirror-reflection symmetry for a 3D PC waveguide, and classify the field symmetry behind the guided modes. In Sec. II we first discuss the solution of Maxwell's equations in the framework of the TMM under mirror-reflection symmetries along one or two directions. In Sec. III we turn to the plane-wave-based TMM, and further explore the symmetric relations between the plane-wave coefficients resulting from the field symmetry of an eigenmode. Maxwell's equations in this irreducible plane-wave space will be solved. With the solution of these symmetry-reduced eigenmodes at hand, in Sec. IV we go on to construct the transfer

matrix that is on the very basis of the TMM. In Sec. V we extend the discussion to a system involving perfectly matched layers (PML's) (Refs. 26 and 36) in order to model absorbing boundary conditions that are necessary to realize the physical solution to the wave problems for a 3D PC waveguide without a complete optical confinement. After having settled down the theoretical basis, we will go on to discuss guided modes in layer-by-layer PC waveguides and 2D PC slab waveguides. In Sec. VI we first investigate the 2D PC slab waveguide. In particular, we focus on waveguides formed in a triangular lattice of air holes etched into an air-bridge dielectric slab. We will make comparison between the TMM calculation and the previous results obtained by the PWM and FDTD simulations. In Sec. VII we turn to 3D waveguides brought into a layer-by-layer photonic crystal. We will compare our results with both the previous theoretical simulations and a recent experimental measurement in the microwave regime. In Sec. VIII we further briefly discuss how the structural symmetries can be of help in understanding the coupling of the PC waveguides with external sources. Finally in Sec. IX we will summarize and conclude this paper.

II. FIELD SYMMETRY UNDER MIRROR-REFLECTION SYMMETRIES IN TMM

The TMM has been extensively studied in the past decades. Different formulations have been presented within the same theoretical framework. We will confine our discussion to the plane-wave-based TMM that we devised recently.[27,28] The principle of this method can be described briefly as follows. First, divide a photonic crystal slab into a number of thin slices, and approximate each slice as a lamellar 2D grating, within which the dielectric function is constant along the *z*-axis direction, the wave propagation direction. Second, surround each slice by an infinitely thin air film in the both hand sides, and write the EM fields in these air films in terms of plane waves consistent with the lattice structure in the cross-sectional plane (the *XY* plane) of the waveguide. Third, solve the eigenmode within each lamellar grating slice under the plane-wave basis, and construct the transfer-matrix connecting the EM fields in the two air films. Fourth, construct the overall transfer matrix for the slab from all individual transfer matrices by means of an iteration algorithm. Finally, calculate from this overall transfer matrix all interesting physical quantities such as the transmission and reflection spectra for a finite slab, or the photonic band structures for an infinite photonic crystal. The principles also apply to a PC waveguide if a supercell in the *XY* plane is used.

To see how structural symmetries may be appreciated in solution of Maxwell's equations, let us first consider a general isotropic structure with modulation in both the permittivity $\epsilon(\mathbf{r})$ and the permeability $\mu(\mathbf{r})$. Although the usual photonic structures are built from nonmagnetic materials, where $\mu(\mathbf{r})=1$ everywhere, we will assume here a general permeability $\mu(\mathbf{r})$ for the sake of later discussion on solution to the wave propagation problem in integrated optical elements, where the PML is introduced in order to model the absorbing boundary conditions similar to those used in the FDTD technique. The PML is made of materials which are anisotropic in the modulation of both $\epsilon(\mathbf{r})$ and $\mu(\mathbf{r})$.

For an isotropic material Maxwell's equations are

$$\nabla\times\mathbf{E}(\mathbf{r})=ik_0\mu(\mathbf{r})\mathbf{H}(\mathbf{r}),\quad \nabla\times\mathbf{H}(\mathbf{r})=-ik_0\epsilon(\mathbf{r})\mathbf{E}(\mathbf{r}). \tag{2.1}$$

Here $k_0=\omega/c$ is the wave number, with c being the light speed in vacuum, and ω the angular frequency of the EM wave. In usual photonic structures, the composite materials are nonmagnetic, and $\mu(\mathbf{r})=1$. But for the time being, we assume a general case where both $\epsilon(\mathbf{r})$ and $\mu(\mathbf{r})$ are spatially varying functions, and possess same mirror-reflection symmetries. Let us first look at the mirror-reflection symmetry with respect to the x axis, where we have $\epsilon(x,y,z)=\epsilon(-x,y,z)$, and $\mu(x,y,z)=\mu(-x,y,z)$. To see the consequence of this symmetry to the solution of Maxwell's equations, we follow the convention of the TMM[28] and rewrite Maxwell's equations into the following four coupled differential equations satisfied by the tangential field components E_x, E_y, H_x, and H_y:

$$\frac{\partial}{\partial z}E_x=\frac{1}{-ik_0}\frac{\partial}{\partial x}\left[\frac{1}{\epsilon}\left(\frac{\partial}{\partial x}H_y-\frac{\partial}{\partial y}H_x\right)\right]+ik_0\mu H_y, \tag{2.2}$$

$$\frac{\partial}{\partial z}E_y=\frac{1}{-ik_0}\frac{\partial}{\partial y}\left[\frac{1}{\epsilon}\left(\frac{\partial}{\partial x}H_y-\frac{\partial}{\partial y}H_x\right)\right]-ik_0\mu H_x, \tag{2.3}$$

$$\frac{\partial}{\partial z}H_x=\frac{1}{ik_0}\frac{\partial}{\partial x}\left[\frac{1}{\mu}\left(\frac{\partial}{\partial x}E_y-\frac{\partial}{\partial y}E_x\right)\right]-ik_0\epsilon E_y, \tag{2.4}$$

$$\frac{\partial}{\partial z}H_y=\frac{1}{ik_0}\frac{\partial}{\partial y}\left[\frac{1}{\mu}\left(\frac{\partial}{\partial x}E_y-\frac{\partial}{\partial y}E_x\right)\right]+ik_0\epsilon E_x. \tag{2.5}$$

In deriving Eqs. (2.2)–(2.5), we have deleted perpendicular field components E_z and H_z from Maxwell's equations, and used the fact that $E_z=[1/(-ik_0\epsilon)](\partial H_y/\partial x-\partial H_x/\partial y)$ and $H_z=[1/(ik_0\mu)](\partial E_y/\partial x-\partial E_x/\partial y)$.

Taking into account the mirror-reflection symmetry, we make coordinate transformations

$$x\rightarrow -x',\quad y\rightarrow y',\quad z\rightarrow z',$$

under which Eqs. (2.2)–(2.5) becomes

$$\frac{\partial}{\partial z'}E_x=\frac{1}{-ik_0}\frac{\partial}{\partial x'}\left[\frac{1}{\epsilon}\left(\frac{\partial}{\partial x'}H_y+\frac{\partial}{\partial y'}H_x\right)\right]+ik_0\mu H_y, \tag{2.6}$$

$$\frac{\partial}{\partial z'}E_y=\frac{1}{-ik_0}\frac{\partial}{\partial y'}\left[\frac{1}{\epsilon}\left(-\frac{\partial}{\partial x'}H_y-\frac{\partial}{\partial y'}H_x\right)\right]-ik_0\mu H_x, \tag{2.7}$$

$$\frac{\partial}{\partial z'}H_x=\frac{1}{ik_0}\frac{\partial}{\partial x'}\left[\frac{1}{\mu}\left(\frac{\partial}{\partial x'}E_y+\frac{\partial}{\partial y'}E_x\right)\right]-ik_0\epsilon E_y, \tag{2.8}$$

$$\frac{\partial}{\partial z'}H_y=\frac{1}{ik_0}\frac{\partial}{\partial y'}\left[\frac{1}{\mu}\left(-\frac{\partial}{\partial x'}E_y-\frac{\partial}{\partial y'}E_x\right)\right]+ik_0\epsilon E_x. \tag{2.9}$$

The EM fields (E_x',E_y',H_x',H_y') in the coordinate system (x',y',z') should satisfy the same Maxwell's equations as Eqs. (2.2)–(2.5). Comparing the sign of each term in Eqs. (2.2)–(2.9), we find that the following two types of transformation for the fields can keep Maxwell's equations invariant:

$$-E_x\rightarrow E_x',\quad E_y\rightarrow E_y',\quad -H_y\rightarrow H_y',\quad H_x\rightarrow H_x' \tag{2.10}$$

and

$$E_x\rightarrow E_x',\quad E_y\rightarrow -E_y',\quad H_y\rightarrow H_y',\quad H_x\rightarrow -H_x'. \tag{2.11}$$

Equations (2.10) and (2.11) can be written in a more explicit way:

$$\begin{aligned}&-E_x(x,y)=E_x(-x,y),\quad E_y(x,y)=E_y(-x,y),\\&-H_y(x,y)=H_y(-x,y),\quad H_x(x,y)=H_x(-x,y),\end{aligned} \tag{2.12}$$

which we call the odd mode for the E_x field under the x-axis mirror-reflection symmetry and

$$\begin{aligned}&E_x(x,y)=E_x(-x,y),\quad E_y(x,y)=-E_y(-x,y),\\&H_y(x,y)=H_y(-x,y),\quad H_x(x,y)=-H_x(-x,y),\end{aligned} \tag{2.13}$$

which we call the even mode for the E_x field under the x-axis mirror-reflection symmetry.

If the structure has a mirror-reflection symmetry with respect to the y axis, namely, $\epsilon(x,y,z)=\epsilon(x,-y,z)$ and $\mu(x,y,z)=\mu(x,-y,z)$, then similarly we can find that the odd and even symmetric modes for the E_x field satisfy

$$\begin{aligned}&-E_x(x,y)=E_x(x,-y),\quad E_y(x,y)=E_y(x,-y),\\&-H_y(x,y)=H_y(x,-y),\quad H_x(x,y)=H_x(x,-y)\end{aligned} \tag{2.14}$$

and

$$\begin{aligned}&E_x(x,y)=E_x(x,-y),\quad E_y(x,y)=-E_y(x,-y),\\&H_y(x,y)=H_y(x,-y),\quad H_x(x,y)=-H_x(x,-y),\end{aligned} \tag{2.15}$$

respectively.

Now further suppose that the structure has mirror-reflection symmetries with respect to both the x and y axes, namely, $\epsilon(x,y,z)=\epsilon(-x,y,z)=\epsilon(x,-y,z)=\epsilon(-x,-y,z)$ and $\mu(x,y,z)=\mu(-x,y,z)=\mu(x,-y,z)=\mu(-x,-y,z)$. We can then combine the results in Eqs. (2.12)–(2.15) and find four different symmetric modes: the even-even, the odd-odd, the even-odd, and the odd-even modes with respect to the E_x field. They have the following symmetric relations:

$$\begin{aligned}&E_x(x,y)=E_x(-x,y)=E_x(x,-y)=E_x(-x,-y),\\&E_y(x,y)=-E_y(-x,y)=-E_y(x,-y)=E_y(-x,-y),\\&H_x(x,y)=-H_x(-x,y)=-H_x(x,-y)=H_x(-x,-y),\\&H_y(x,y)=H_y(-x,y)=H_y(x,-y)=H_y(-x,-y)\end{aligned} \tag{2.16}$$

for the even-even mode,

$$\begin{aligned}&E_x(x,y)=-E_x(-x,y)=-E_x(x,-y)=E_x(-x,-y),\\&E_y(x,y)=E_y(-x,y)=E_y(x,-y)=E_y(-x,-y),\\&H_x(x,y)=H_x(-x,y)=H_x(x,-y)=H_x(-x,-y),\\&H_y(x,y)=-H_y(-x,y)=-H_y(x,-y)=H_y(-x,-y)\end{aligned} \tag{2.17}$$

for the odd-odd mode,

$$\begin{aligned}&E_x(x,y)=E_x(-x,y)=-E_x(x,-y)=-E_x(-x,-y),\\&E_y(x,y)=-E_y(-x,y)=E_y(x,-y)=-E_y(-x,-y),\\&H_x(x,y)=-H_x(-x,y)=H_x(x,-y)=-H_x(-x,-y),\\&H_y(x,y)=H_y(-x,y)=-H_y(x,-y)=-H_y(-x,-y)\end{aligned} \tag{2.18}$$

for the even-odd mode, and

$$\begin{aligned}&E_x(x,y)=-E_x(-x,y)=E_x(x,-y)=-E_x(-x,-y),\\&E_y(x,y)=E_y(-x,y)=-E_y(x,-y)=-E_y(-x,-y),\\&H_x(x,y)=H_x(-x,y)=-H_x(x,-y)=-H_x(-x,-y),\\&H_y(x,y)=-H_y(-x,y)=H_y(x,-y)=-H_y(-x,-y)\end{aligned} \tag{2.19}$$

for the odd-even mode, respectively.

It can be seen that the field symmetry associated with the mirror-reflection structural symmetries exhibits a very compact, concise, and clarified form. This can be attributed to mathematical structure of the TMM, where the investigated field vectors (E_x,E_y) and (H_x,H_y) are collinear with the symmetry axes of the waveguide structure. From Maxwell's equations, one can find that there also exist symmetries in the perpendicular field components E_z and H_z, which can be derived from the symmetric relations involved in the four tangential field components. As E_z and H_z are not relevant in our TMM, we will not discuss this subject in detail. Such beautiful symmetric forms in the field components can help us to solve the EM problems in a convenient and clarified manner that other numerical schemes such as the FDTD technique and the conventional PWM have not yet appreciated.

III. PLANE-WAVE-BASED TMM UNDER MIRROR-REFLECTION SYMMETRIES

In the above section we have obtained the symmetry of the EM fields in the real space in connection with various

mirror-reflection symmetry operations. These symmetric relations can be directly used in the real-space TMM.[23] Since we prefer to use the plane-wave-based TMM,[28] we need to reflect them into the plane-wave space. Let the primitive lattice **R** of the 2D grating in the *XY* plane has two basis vectors $\mathbf{a}_1$ and $\mathbf{a}_2$, and the corresponding reciprocal lattice **G** has two basis vectors $\mathbf{b}_1$ and $\mathbf{b}_2$. In practice, we always choose a rectangular supercell for the waveguide problem, so we have $\mathbf{a}_1 \cdot \mathbf{a}_2 = 0$ and $\mathbf{b}_1 \cdot \mathbf{b}_2 = 0$, namely, the primitive and reciprocal lattices both have orthogonal basis vectors.

The EM fields can be written into the superposition of plane waves (or Bragg waves).

$$\mathbf{E}(\mathbf{r}) = \sum_{ij} \mathbf{E}_{i,j}(z) e^{i(k_{ij,x}x + k_{ij,y}y)}, \tag{3.1}$$

$$\mathbf{H}(\mathbf{r}) = \sum_{ij} \mathbf{H}_{i,j}(z) e^{i(k_{ij,x}x + k_{ij,y}y)}, \tag{3.2}$$

where the Bragg wave vector $\mathbf{k}_{ij} = (k_{ij,x}, k_{ij,y}) = \mathbf{k}_0 + \mathbf{G}_{ij} = (k_{0x}, k_{0y}) + i\mathbf{b}_1 + j\mathbf{b}_2$, $\mathbf{E}_{ij}$ and $\mathbf{H}_{ij}$ are unknown expansion coefficients of the electric and magnetic fields. They are both varying function along the *z*-axis direction. In consistence with the mirror-reflection symmetry involved in the wave propagation problem for a PC waveguide system, we should have $(k_{0x}, k_{0y}) = (0,0)$, and $\mathbf{k}_{ij} = \mathbf{G}_{ij}$.

The symmetric relations in the plane-wave space can be directly obtained from the corresponding relations in the real space. For instance, it is easy to find from Eq. (3.1) that $E_x(x,y) = E_x(-x,y)$ would lead to $E^x_{i,j} = E^x_{-i,j}$. Following the same principle, we can find from Eqs. (2.12) and (2.13) for the *x*-axis mirror-reflection symmetry the following symmetric relations between the plane-wave coefficients:

$$E^x_{i,j} = E^x_{-i,j}, \quad E^y_{i,j} = -E^y_{-i,j},$$
$$H^x_{i,j} = -H^x_{-i,j}, \quad H^y_{i,j} = H^y_{-i,j} \tag{3.3}$$

for the even mode and

$$E^x_{i,j} = -E^x_{-i,j}, \quad E^y_{i,j} = E^y_{-i,j},$$
$$H^x_{i,j} = H^x_{-i,j}, \quad H^y_{i,j} = -H^y_{-i,j} \tag{3.4}$$

for the odd mode. For the *y*-axis mirror-reflection symmetry, we have

$$E^x_{i,j} = E^x_{i,-j}, \quad E^y_{i,j} = -E^y_{i,-j},$$
$$H^x_{i,j} = -H^x_{i,-j}, \quad H^y_{i,j} = H^y_{i,-j} \tag{3.5}$$

for the even mode, and

$$E^x_{i,j} = -E^x_{i,-j}, \quad E^y_{i,j} = E^y_{i,-j},$$
$$H^x_{i,j} = H^x_{i,-j}, \quad H^y_{i,j} = -H^y_{i,-j} \tag{3.6}$$

for the odd mode. In the presence of simultaneous *x* and *y* axis mirror-reflection symmetries, the symmetric relations between the plane-wave coefficients are

$$E^x_{i,j} = E^x_{-i,j} = E^x_{i,-j} = E^x_{-i,-j},$$
$$E^y_{i,j} = -E^y_{-i,j} = -E^y_{i,-j} = E^y_{-i,-j},$$
$$H^x_{i,j} = -H^x_{-i,j} = -H^x_{i,-j} = H^x_{-i,-j},$$
$$H^y_{i,j} = H^y_{-i,j} = H^y_{i,-j} = H^y_{-i,-j} \tag{3.7}$$

for the even-even mode,

$$E^x_{i,j} = -E^x_{-i,j} = -E^x_{i,-j} = E^x_{-i,-j},$$
$$E^y_{i,j} = E^y_{-i,j} = E^y_{i,-j} = E^y_{-i,-j},$$
$$H^x_{i,j} = H^x_{-i,j} = H^x_{i,-j} = H^x_{-i,-j},$$
$$H^y_{i,j} = -H^y_{-i,j} = -H^y_{i,-j} = H^y_{-i,-j} \tag{3.8}$$

for the odd-odd mode,

$$E^x_{i,j} = E^x_{-i,j} = -E^x_{i,-j} = -E^x_{-i,-j},$$
$$E^y_{i,j} = -E^y_{-i,j} = E^y_{i,-j} = -E^y_{-i,-j},$$
$$H^x_{i,j} = -H^x_{-i,j} = H^x_{i,-j} = -H^x_{-i,-j},$$
$$H^y_{i,j} = H^y_{-i,j} = -H^y_{i,-j} = -H^y_{-i,-j} \tag{3.9}$$

for the even-odd mode, and

$$E^x_{i,j} = -E^x_{-i,j} = E^x_{i,-j} = -E^x_{-i,-j},$$
$$E^y_{i,j} = E^y_{-i,j} = -E^y_{i,-j} = -E^y_{-i,-j},$$
$$H^x_{i,j} = H^x_{-i,j} = -H^x_{i,-j} = -H^x_{-i,-j},$$
$$H^y_{i,j} = -H^y_{-i,j} = H^y_{i,-j} = -H^y_{-i,-j} \tag{3.10}$$

for the odd-even mode. All symmetric modes are named in reference to the E_x field.

Now that we have obtained the symmetric relations among different plane-wave coefficients, we can proceed to utilize these relations to simplify the solution of the wave propagation problem in the framework of the TMM. For a general photonic structure without any structural symmetry consideration, substituting the EM fields (3.1) and (3.2) into Maxwell's equations (2.2)–(2.5) will lead to the following compact matrix form of coupled differential equations[28]

$$\frac{\partial}{\partial z} E = T_1 H, \quad \frac{\partial}{\partial z} H = T_2 E, \tag{3.11}$$

where *E* and *H* are both column vectors consisting of the plane-wave coefficients and they are defined by

$$E = (\ldots, E^x_{i,j}, E^y_{i,j}, \ldots)^T,$$
$$H = (\ldots, H^x_{i,j}, H^y_{i,j}, \ldots)^T,$$

with *T* denoting the matrix transposition. The matrices T_1 and T_2 have their matrix elements defined as

$$T^{x;x}_{1;i,j;m,n} = ik_{ij,x}[\epsilon_z]^{-1}_{ij;mn}k_{mn,y}/k_0,$$

$$T^{x;y}_{1;i,j;m,n} = i(-k_{ij,x}[\epsilon_z]^{-1}_{ij;mn}k_{mn,x} + k_0^2[\mu_y]_{ij;mn})/k_0,$$

$$T^{y;x}_{1;i,j;m,n} = i(k_{ij,y}[\epsilon_z]^{-1}_{ij;mn}k_{mn,y} - k_0^2[\mu_x]_{ij;mn})/k_0,$$

$$T^{y;y}_{1;i,j;m,n} = -ik_{ij,y}[\epsilon_z]^{-1}_{ij;mn}k_{mn,x}/k_0 \tag{3.12}$$

and

$$T^{x;x}_{2;i,j;m,n} = -ik_{ij,x}[\mu_z]^{-1}_{ij;mn}k_{mn,y}/k_0,$$

$$T^{x;y}_{2;i,j;m,n} = i(k_{ij,x}[\mu_z]^{-1}_{ij;mn}k_{mn,x} - k_0^2[\epsilon_y]_{ij;mn})/k_0,$$

$$T^{y;x}_{2;i,j;m,n} = i(-k_{ij,y}[\mu_z]^{-1}_{ij;mn}k_{mn,y} + k_0^2[\epsilon_x]_{ij;mn})/k_0,$$

$$T^{y;y}_{2;i,j;m,n} = ik_{ij,y}[\mu_z]^{-1}_{ij;mn}k_{mn,x}/k_0. \tag{3.13}$$

If $(2N_1+1)\times(2N_2+1)=N$ plane waves are used to expand the EM fields, then the dimension of E and H is both $2N$, while the matrices T_1 and T_2 both are of dimension $(2N)\times(2N)$. The material-related Fourier-coefficient matrices $[\epsilon_z]$ etc. in T_1 and T_2 all have dimension of $N\times N$. Note that the designation of different subscripts x,y,z in the Fourier matrices $[\epsilon]$ and $[\mu]$ is used to represent different Fourier expansion rules that are employed to calculate these material-related matrix elements in order to obtain optimum numerical convergence. According to Ref. 25, $[\epsilon_z]^{-1}_{ij;mn}$ and $[\mu_z]^{-1}_{ij;mn}$ in Eqs. (3.12) and (3.13) are calculated by using the inverse rule, namely, we first solve $[\epsilon_z]_{ij;mn}$ and $[\mu_z]_{ij;mn}$, then perform the matrix inversion, leading to $[\epsilon_z]^{-1}_{ij;mn}$ and $[\mu_z]^{-1}_{ij;mn}$. Explicitly we have

$$[\epsilon_z]_{ij;mn} = [\epsilon_z]_{i-m,j-n} = \frac{1}{d_1 d_2}\int_{-d_1/2}^{d_1/2}\int_{-d_2/2}^{d_2/2}\epsilon(x,y) \times e^{-i(k_{ij,x}-k_{mn,x})x - i(k_{ij,y}-k_{mn,y})y}dxdy, \tag{3.14}$$

$$[\mu_z]_{ij;mn} = [\mu_z]_{i-m,j-n} = \frac{1}{d_1 d_2}\int_{-d_1/2}^{d_1/2}\int_{-d_1/2}^{d_2/2}\mu(x,y) \times e^{-i(k_{ij,x}-k_{mn,x})x - i(k_{ij,y}-k_{mn,y})y}dxdy, \tag{3.15}$$

where d_1 and d_2 are the lattice constant along the x and y directions, respectively, $k_{ij,x}-k_{mn,x}=(i-m)(2\pi/d_1)$, $k_{ij,y}-k_{mn,y}=(j-n)(2\pi/d_2)$. The optimal Fourier expansion rules for the other matrices $[\epsilon_x]$, $[\epsilon_y]$, $[\mu_x]$, and $[\mu_y]$ are more complicated, and all involve a mixture of the direct and inverse rules. They are given by

$$[\epsilon_y]_{ij;mn} = \frac{1}{d_1}\int_{-d_1/2}^{d_1/2}\{[1/\epsilon]^{-1}_{j,n}\}(x)e^{-i(k_{ij,x}-k_{mn,x})x}dx, \tag{3.16}$$

$$[\epsilon_x]_{ij;mn} = \frac{1}{d_2}\int_{-d_2/2}^{d_2/2}\{[1/\epsilon]^{-1}_{i,m}\}(y)e^{-i(k_{ij,y}-k_{mn,y})y}dy, \tag{3.17}$$

$$[\mu_y]_{ij;mn} = \frac{1}{d_1}\int_{-d_1/2}^{d_1/2}\{[1/\mu]^{-1}_{j,n}\}(x)e^{-i(k_{ij,x}-k_{mn,x})x}dx, \tag{3.18}$$

$$[\mu_x]_{ij;mn} = \frac{1}{d_2}\int_{-d_2/2}^{d_2/2}\{[1/\mu]^{-1}_{i,m}\}(y)e^{-i(k_{ij,y}-k_{mn,y})y}dy. \tag{3.19}$$

Here we have assumed that the coordinate origin is located at the center of the supercell. The matrix $[1/\epsilon]^{-1}_{j,n}(x)$ is the inversion of the matrix $[1/\epsilon]_{j,n}(x)$, and so on. The latter matrices are calculated by means of the direct Fourier expansion rule and are given by

$$[1/\epsilon]_{j,n}(x) = \frac{1}{d_2}\int_{-d_2/2}^{d_2/2}\left[\frac{1}{\epsilon(x,y)}\right]e^{-i(k_{ij,y}-k_{mn,y})y}dy, \tag{3.20}$$

$$[1/\epsilon]_{i,m}(y) = \frac{1}{d_1}\int_{-d_1/2}^{d_1/2}\left[\frac{1}{\epsilon(x,y)}\right]e^{-i(k_{ij,x}-k_{mn,x})x}dx, \tag{3.21}$$

$$[1/\mu]_{j,n}(x) = \frac{1}{d_2}\int_{-d_2/2}^{d_2/2}\left[\frac{1}{\mu(x,y)}\right]e^{-i(k_{ij,y}-k_{mn,y})y}dy, \tag{3.22}$$

$$[1/\mu]_{i,m}(y) = \frac{1}{d_1}\int_{-d_1/2}^{d_1/2}\left[\frac{1}{\mu(x,y)}\right]e^{-i(k_{ij,x}-k_{mn,x})x}dx. \tag{3.23}$$

For a usual photonic structure built from nonmagnetic materials, $\mu(x,y)=1$ everywhere. Then we can easily find that the Fourier matrices $[\mu_x]$, $[\mu_y]$, and $[\mu_z]$ are all unity matrices. Then Eqs. (3.12) and (3.13) become

$$T^{x;x}_{1;i,j;m,n} = ik_{ij,x}[\epsilon_z]^{-1}_{ij;mn}k_{mn,y}/k_0,$$

$$T^{x;y}_{1;i,j;m,n} = i(-k_{ij,x}[\epsilon_z]^{-1}_{ij;mn}k_{mn,x} + k_0^2\delta_{ij;mn})/k_0,$$

$$T^{y;x}_{1;i,j;m,n} = i(k_{ij,y}[\epsilon_z]^{-1}_{ij;mn}k_{mn,y} - k_0^2\delta_{ij;mn})/k_0,$$

$$T^{y;y}_{1;i,j;m,n} = -ik_{ij,y}[\epsilon_z]^{-1}_{ij;mn}k_{mn,x}/k_0 \tag{3.24}$$

and

$$T^{x;x}_{2;i,j;m,n} = -ik_{ij,x}[\mu_z]^{-1}_{ij;mn}k_{mn,y}/k_0,$$

$$T^{x;y}_{2;i,j;m,n} = i(k_{ij,x}\delta_{ij;mn}k_{mn,x} - k_0^2[\epsilon_y]_{ij;mn})/k_0,$$

$$T^{y;x}_{2;i,j;m,n} = i(-k_{ij,y}\delta_{ij;mn}k_{mn,y} + k_0^2[\epsilon_x]_{ij;mn})/k_0,$$

$$T^{y;y}_{2;i,j;m,n} = ik_{ij,y}[\mu_z]^{-1}_{ij;mn}k_{mn,x}/k_0. \tag{3.25}$$

One can find that the Fourier matrices in Eqs. (3.14)–(3.20) are all Toeplitz matrices characterized by symmetry relations $A_{ij}=A_{i-j}$ and $B_{ij;mn}=B_{i-m;j-n}$. This symmetry can significantly reduce the number of independent matrix elements, and thus help to greatly release the computational burden to calculate these matrices. In our numerical practice, we discretize the supercell into a number of rectangular minicells. The permittivity and permeability in each minicell are represented by constants obtained by averaging over $\epsilon(x,y)$ and $\mu(x,y)$ in the cell. Then the Fourier matrices are numerically calculated by summing up contributions from all minicells to the integration in Eqs. (3.14)–(3.23).

From Eq. (3.11) we can derive an eigenproblem for the electric field

$$\frac{\partial^2}{\partial z^2}E = (T_1T_2)E = -PE \tag{3.26}$$

or in a more explicit and expanded form,

$$\frac{\partial^2}{\partial z^2}\begin{pmatrix} E^x_{i,j} \\ E^y_{i,j} \end{pmatrix} = -P^{\lambda_1;\lambda_2}_{i,j;m,n}\begin{pmatrix} E^x_{m,n} \\ E^y_{m,n} \end{pmatrix}. \tag{3.27}$$

The superscripts λ_1 and λ_2 are polarization indices x and y, while the indices appearing in the subscript represent the plane wave used, and run in the range of $-N_1 \leqslant i \leqslant N_1$, $-N_2 \leqslant j \leqslant N_2$, $-N_1 \leqslant m \leqslant N_1$, $-N_2 \leqslant n \leqslant N_2$. The total plane wave number is $N=(2N_1+1)(2N_2+1)$. Equation (3.27) should be understood as a matrix second-order differential equation. The solution of the eigenproblem within each slice centered at z will yield the eigenmodes of the EM fields within this approximate lamellar 2D grating slice. These eigenmodes will stand on the basis of constructing the transfer matrix for this slice.

If the structure has a certain mirror-reflection symmetry, there are definite symmetric relations among the plane-wave coefficients. We can use the symmetry to pick up those independent unknown variables of the plane-wave coefficients and regroup Eq. (3.27). For the x-axis mirror-reflection symmetry, we confine the used plane waves in the range of $0 \leqslant i \leqslant N_1$, $-N_2 \leqslant j \leqslant N_2$, $0 \leqslant m \leqslant N_1$, $-N_2 \leqslant n \leqslant N_2$, and rewrite Eq. (3.27) as

$$\frac{\partial^2}{\partial z^2}\begin{pmatrix} E^x_{i,j} \\ E^y_{i,j} \end{pmatrix} = -Q^{\lambda_1;\lambda_2}_{i,j;m,n}\begin{pmatrix} E^x_{m,n} \\ E^y_{m,n} \end{pmatrix}, \tag{3.28}$$

where

$$Q^{\lambda_1;\lambda_2}_{i,j;m,n} = P^{\lambda_1;\lambda_2}_{i,j;m,n} + \hat{P}^{\lambda_1;\lambda_2}_{i,j;-m,n}\Theta(m-1).$$

$M=(N_1+1)\times(2N_2+1)$ is the plane wave used in the calculation, and the matrix Q has a dimension of $(2M)\times(2M)$. The term $\hat{P}^{\lambda_1;\lambda_2}_{i,j;-m,n}$ represents the contribution from those plane waves with $k_x<0$. The attached factor $\Theta(m-1)$ is defined as $\Theta(m-1)=1$ if $m \geqslant 1$, and $\Theta(m-1)=0$ if $m<1$. This factor is used to avoid unphysical dual counting of these terms of $\hat{P}^{\lambda_1;\lambda_2}_{i,j;0,n}$. We note that $\hat{P}^{\lambda_1;\lambda_2}_{i,j;-m,n}$ has included a sign factor of "+" or "−," which comes from the symmetric relations (3.3) and (3.4). This term should depend on the symmetric mode concerned. For instance, for the even mode, $\hat{P}^{x(y);x}_{i,j;-m,n} = P^{x(y);x}_{i,j;-m,n}$, $\hat{P}^{x(y);y}_{i,j;-m,n} = -P^{x(y);y}_{i,j;-m,n}$, while for the odd mode, we have $\hat{P}^{x(y);x}_{i,j;-m,n} = -P^{x(y);x}_{i,j;-m,n}$ and $\hat{P}^{x(y);y}_{i,j;-m,n} = P^{x(y);y}_{i,j;-m,n}$.

In the case of the y-axis mirror-reflection symmetry, Eq. (3.27) becomes

$$\frac{\partial^2}{\partial z^2}\begin{pmatrix} E^x_{i,j} \\ E^y_{i,j} \end{pmatrix} = -Q^{\lambda_1;\lambda_2}_{i,j;m,n}\begin{pmatrix} E^x_{m,n} \\ E^y_{m,n} \end{pmatrix}, \tag{3.29}$$

where

$$Q^{\lambda_1;\lambda_2}_{i,j;m,n} = P^{\lambda_1;\lambda_2}_{i,j;m,n} + \hat{P}^{\lambda_1;\lambda_2}_{i,j;m,-n}\Theta(n-1),$$

where the plane waves used are confined to $-N_1 \leqslant i \leqslant N_1$, $0 \leqslant j \leqslant N_2$, $-N_1 \leqslant m \leqslant N_1$, $0 \leqslant n \leqslant N_2$, and the total number is $M=(2N_1+1)\times(N_2+1)$. The factor $\Theta(n-1)$ is defined as $\Theta(n-1)=1$ if $n \geqslant 1$, and $\Theta(n-1)=0$ if $n<1$. This factor is also used to avoid unphysical dual counting of these terms of $\hat{P}^{\lambda_1;\lambda_2}_{i,j;m,0}$. $\hat{P}^{\lambda_1;\lambda_2}_{i,j;m,-n}$ also depend on the symmetric mode concerned. When the structure has both the x and y axis mirror-reflection symmetries, Eq. (3.27) can be much more simplified. Now the plane waves used are confined to $0 \leqslant i \leqslant N_1$, $0 \leqslant j \leqslant N_2$, $0 \leqslant m \leqslant N_1$, $0 \leqslant n \leqslant N_2$ with a total number of $M=(N_1+1)\times(N_2+1)$. Eq. (3.27) becomes

$$\frac{\partial^2}{\partial z^2}\begin{pmatrix} E^x_{i,j} \\ E^y_{i,j} \end{pmatrix} = -Q^{\lambda_1;\lambda_2}_{i,j;m,n}\begin{pmatrix} E^x_{m,n} \\ E^y_{m,n} \end{pmatrix}, \tag{3.30}$$

where

$$Q^{\lambda_1;\lambda_2}_{i,j;m,n} = P^{\lambda_1;\lambda_2}_{i,j;m,n} + \hat{P}^{\lambda_1;\lambda_2}_{i,j;-m,n}\Theta(m-1) + \hat{P}^{\lambda_1;\lambda_2}_{i,j;m,-n}\Theta(n-1) + \hat{P}^{\lambda_1;\lambda_2}_{i,j;-m,-n}\Theta(m-1)\Theta(n-1).$$

The last three terms in $Q^{\lambda_1;\lambda_2}_{i,j;m,n}$ should also depend on the symmetric mode under study.

In constructing the transfer matrix for a slice, the boundary condition satisfied by the **H** field is required. The **H** field is connected with the **E** field through Eq. (3.11). For a general structure, we can write

$$\frac{\partial}{\partial z}\begin{pmatrix} E^x_{i,j} \\ E^y_{i,j} \end{pmatrix} = T^{\lambda_1;\lambda_2}_{1;i,j;m,n}\begin{pmatrix} H^x_{m,n} \\ H^y_{m,n} \end{pmatrix}, \tag{3.31}$$

where the indices range in $-N_1 \leqslant i \leqslant N_1$, $-N_2 \leqslant j \leqslant N_2$, $-N_1 \leqslant m \leqslant N_1$, $-N_2 \leqslant n \leqslant N_2$. When the structure has mirror-reflection symmetries, Eq. (3.31) can regroup in a way similar to Eq. (3.27) such that only independent un-

known variables of the plane-wave coefficients enter the new equations. For all types of symmetry, we can write down

$$\frac{\partial}{\partial z}\begin{pmatrix} E^x_{i,j} \\ E^y_{i,j} \end{pmatrix} = R^{\lambda_1;\lambda_2}_{i,j;m,n}\begin{pmatrix} H^x_{m,n} \\ H^y_{m,n} \end{pmatrix}. \tag{3.32}$$

The reduced matrix R depends on what symmetry is involved with. For the x-axis mirror-reflection symmetry

$$R^{\lambda_1;\lambda_2}_{i,j;m,n} = T^{\lambda_1;\lambda_2}_{1;i,j;m,n} + \hat{T}^{\lambda_1;\lambda_2}_{1;i,j;-m,n}\Theta(m-1). \tag{3.33}$$

For the y-axis mirror-reflection symmetry,

$$R^{\lambda_1;\lambda_2}_{i,j;m,n} = T^{\lambda_1;\lambda_2}_{1;i,j;m,n} + \hat{T}^{\lambda_1;\lambda_2}_{1;i,j;m,-n}\Theta(n-1). \tag{3.34}$$

When the structure has simultaneous x and y mirror-reflection symmetries, we find

$$R^{\lambda_1;\lambda_2}_{i,j;m,n} = T^{\lambda_1;\lambda_2}_{1;i,j;m,n} + \hat{T}^{\lambda_1;\lambda_2}_{1;i,j;-m,n}\Theta(m-1) + \hat{T}^{\lambda_1;\lambda_2}_{1;i,j;m,-n} \times\Theta(n-1) + \hat{T}^{\lambda_1;\lambda_2}_{1;i,j;-m,-n}\Theta(m-1)\Theta(n-1). \tag{3.35}$$

The matrix R in Eq. (3.33) has the same dimension as the matrix Q in Eq. (3.28), and so on. The calculation of these matrices should also depend on the symmetric modes concerned in the wave propagation problem. For instance, under the x-axis mirror-reflection symmetry, we have $\hat{T}^{x(y);x}_{1;i,j;-m,n} = -T^{x(y);x}_{1;i,j;-m,n}$ and $\hat{T}^{x(y);y}_{1;i,j;-m,n} = T^{x(y);y}_{1;i,j;-m,n}$ for the even mode, while for the odd mode we have $\hat{T}^{x(y);x}_{1;i,j;-m,n} = T^{x(y);x}_{1;i,j;-m,n}$ and $\hat{T}^{x(y);y}_{1;i,j;-m,n} = -T^{x(y);y}_{1;i,j;-m,n}$. Others are similarly defined.

Above we employ the structural symmetries to reduce the number of independent plane-wave coefficients appearing in Maxwell's equations. This can significantly ease the numerical burden and the requirement on computer memory space. However, a closer look at the symmetrical relations (3.3)–(3.10) and the eigenproblems (3.28)–(3.30) show that we have not yet arrived at the truly irreducible plane-wave space that is needed in solution of these symmetry-related EM problems. The reason is that some symmetry-induced constant-zero variables are still involved in Eqs. (3.28)–(3.30). This will lead to superfluous unphysical solutions of the eigenproblem. This situation can be seen from the dimension of the matrices in these equations. One way to remove these parasite modes is to check the eigenvector. Those eigenvectors that do not satisfy the particular symmetric relations consistent with the structural symmetry will correspond to unphysical solutions, and should be excluded. However, another simpler while more efficient way is to remove these constant-zero variables from Maxwell's equations (3.28)–(3.30) from the beginning. In the following we will show how to achieve this goal.

Let us first look at the situation of the x-axis mirror-reflection symmetry. From Eqs. (3.3) and (3.4), we can find that

$$E^y_{0,j} = 0, \quad H^x_{0,j} = 0$$

for the even mode and

$$E^x_{0,j} = 0, \quad H^y_{0,j} = 0$$

for the odd mode. These symmetry-induced constant-zero variables should be removed from Maxwell's equations (3.27) and (3.32). Accordingly, the involved matrices Q and R should contract by removing those elements that are related with $E^y_{0,j}$ and $H^x_{0,j}$ such as $Q^{y;y}_{0,j;0,n}$ and $R^{y;x}_{0,j;0,n}$ for the even mode, and those elements that are related with $E^x_{0,j}$ and $H^y_{0,j}$ such as $Q^{x;x}_{0,j;0,n}$ and $R^{x;y}_{0,j;0,n}$ for the odd mode. After exclusion of these $2N_2+1$ constant-zero variables, the new total number of the independent variables will reduce from $2(N_1+1)(2N_2+1)$ to $(2N_1+1)\times(2N_2+1) = N$, which is also the dimension of Q and R. This we see that the new eigenproblem has a size half of the original one, which is $2N$. In a more explicit form, Eq. (3.28) can be written into

$$\frac{\partial^2}{\partial z^2}\begin{pmatrix} E^x_{0,j} \\ E^x_{i,j} \\ E^y_{i,j} \end{pmatrix} = -\begin{pmatrix} Q^{x;x}_{0,j;0,n} & Q^{x;x}_{0,j;m,n} & Q^{x;y}_{0,j;m,n} \\ Q^{x;x}_{i,j;0,n} & Q^{x;x}_{i,j;m,n} & Q^{x;y}_{i,j;m,n} \\ Q^{y;x}_{i,j;0,n} & Q^{y;x}_{i,j;m,n} & Q^{y;y}_{i,j;m,n} \end{pmatrix}\begin{pmatrix} E^x_{0,n} \\ E^x_{m,n} \\ E^y_{m,n} \end{pmatrix} \tag{3.36}$$

for the even mode and

$$\frac{\partial^2}{\partial z^2}\begin{pmatrix} E^y_{0,j} \\ E^x_{i,j} \\ E^y_{i,j} \end{pmatrix} = -\begin{pmatrix} Q^{y;y}_{0,j;0,n} & Q^{y;x}_{0,j;m,n} & Q^{y;y}_{0,j;m,n} \\ Q^{x;y}_{i,j;0,n} & Q^{x;x}_{i,j;m,n} & Q^{x;y}_{i,j;m,n} \\ Q^{y;y}_{i,j;0,n} & Q^{y;x}_{i,j;m,n} & Q^{y;y}_{i,j;m,n} \end{pmatrix}\begin{pmatrix} E^y_{0,n} \\ E^x_{m,n} \\ E^y_{m,n} \end{pmatrix} \tag{3.37}$$

for the odd mode, respectively. On the other hand, Eq. (3.32) now takes an explicit form

$$\frac{\partial}{\partial z}\begin{pmatrix} E^x_{0,j} \\ E^x_{i,j} \\ E^y_{i,j} \end{pmatrix} = \begin{pmatrix} R^{x;y}_{0,j;0,n} & R^{x;x}_{0,j;m,n} & R^{x;y}_{0,j;m,n} \\ R^{x;y}_{i,j;0,n} & R^{x;x}_{i,j;m,n} & R^{x;y}_{i,j;m,n} \\ R^{y;y}_{i,j;0,n} & R^{y;x}_{i,j;m,n} & R^{y;y}_{i,j;m,n} \end{pmatrix}\begin{pmatrix} H^y_{0,n} \\ H^x_{m,n} \\ H^y_{m,n} \end{pmatrix} \tag{3.38}$$

for the even mode and

$$\frac{\partial}{\partial z}\begin{pmatrix} E^y_{0,j} \\ E^x_{i,j} \\ E^y_{i,j} \end{pmatrix} = \begin{pmatrix} R^{y;x}_{0,j;0,n} & R^{y;x}_{0,j;m,n} & R^{y;y}_{0,j;m,n} \\ R^{x;x}_{i,j;0,n} & R^{x;x}_{i,j;m,n} & R^{x;y}_{i,j;m,n} \\ R^{y;x}_{i,j;0,n} & R^{y;x}_{i,j;m,n} & R^{y;y}_{i,j;m,n} \end{pmatrix}\begin{pmatrix} H^x_{0,n} \\ H^x_{m,n} \\ H^y_{m,n} \end{pmatrix} \tag{3.39}$$

for the odd mode, respectively. In Eqs. (3.36)–(3.39), the indices run as $1 \leqslant i \leqslant N_1$, $1 \leqslant m \leqslant N_1$, $-N_2 \leqslant j \leqslant N_2$, and $-N_2 \leqslant n \leqslant N_2$. Each matrix element should be understood as a block submatrix.

The situation of the y-axis mirror-reflection symmetry can be handled in a similar way. From Eqs. (3.5) and (3.6), we can find that

$$E^y_{i,0} = 0, \quad H^x_{i,0} = 0$$

for the even mode and

$$E^x_{i,0} = 0, \quad H^y_{i,0} = 0$$

for the odd mode. After removing these constant-zero matrix elements, the matrices Q and R should contract accordingly by removing those elements of $Q^{y;y}_{i,0;m,0}$, $R^{y;x}_{i,0;m,0}$, etc., for the even mode and $Q^{x;x}_{i,0;m,0}$ and $R^{x;y}_{i,0;m,0}$, etc., for the odd mode. In the end, Q and R will also have a size of N for both modes. The explicit form of Eqs. (3.29) and (3.32) can be written in a similar way as Eqs. (3.36)–(3.39).

The situation of simultaneous x and y mirror-reflection symmetries is somewhat more complex. Let us first look at the even-even mode. From the symmetric relations shown in Eq. (3.7), we easily find that

$$E^y_{0,j}=E^y_{i,0}=0,\quad H^x_{0,j}=H^x_{i,0}=0.$$

This means that we should exclude these constant-zero **E** and **H** field variables, whose total number is both N_1+N_2+1. Then the truly independent unknown variables have a total number of $M=2(N_1+1)(N_2+1)-(N_1+N_2+1)=\frac{1}{2}[(2N_1+1)(2N_2+1)+1]=\frac{1}{2}(N+1)$, about one quarter of the original dimension without any symmetry consideration. The matrix Q in Eq. (3.30) and R in Eq. (3.32) should be contracted accordingly such that those matrix elements of $Q^{y;y}_{0,j;0,n}$, $Q^{y;y}_{i,0;m,0}$, $R^{y;x}_{0,j;0,n}$, $R^{y;x}_{i,0;m,0}$, etc., are removed. Both matrices now have a dimension of $M\times M$. For the odd-odd mode, we have

$$E^x_{0,j}=E^x_{i,0}=0,\quad H^y_{0,j}=H^y_{i,0}=0.$$

The independent unknown variables are reduced to a total number of $M=\frac{1}{2}(N+1)$, same as in the even-even mode. Correspondingly, the matrix elements of $Q^{x;x}_{0,j;0,n}$, $Q^{x;x}_{i,0;m,0}$, $R^{x;y}_{0,j;0,n}$, $R^{x;y}_{i,0;m,0}$, etc., should be removed, yielding a new eigenproblem with a size of M. One can write down the explicit form of Eqs. (3.30) and (3.32) under these two symmetries in a way similar to but much more complicated than Eqs. (3.36)–(3.39) for the x-axis symmetry case. For instance, for the even-even mode, Eqs. (3.30) and (3.32) can be expanded into

$$\frac{\partial^2}{\partial z^2}\begin{pmatrix} E^x_{0,0}\\ E^x_{0,j}\\ E^x_{i,0}\\ E^x_{i,j}\\ E^y_{i,j}\end{pmatrix} = -\begin{pmatrix} Q^{x;x}_{0,0;0,0} & Q^{x;x}_{0,0;0,n} & Q^{x;x}_{0,0;m,0} & Q^{x;x}_{0,0;m,n} & Q^{x;y}_{0,0;m,n}\\ Q^{x;x}_{0,j;0,0} & Q^{x;x}_{0,j;0,n} & Q^{x;x}_{0,j;m,0} & Q^{x;x}_{0,j;m,n} & Q^{x;y}_{0,j;m,n}\\ Q^{x;x}_{i,0;0,0} & Q^{x;x}_{i,0;0,n} & Q^{x;x}_{i,0;m,0} & Q^{x;x}_{i,0;m,n} & Q^{x;y}_{i,0;m,n}\\ Q^{x;x}_{i,j;0,0} & Q^{x;x}_{i,j;0,n} & Q^{x;x}_{i,j;m,0} & Q^{x;x}_{i,j;m,n} & Q^{x;y}_{i,j;m,n}\\ Q^{y;x}_{i,j;0,0} & Q^{y;x}_{i,j;0,n} & Q^{y;x}_{i,j;m,0} & Q^{y;x}_{i,j;m,n} & Q^{y;y}_{i,j;m,n}\end{pmatrix} \times\begin{pmatrix} E^x_{0,0}\\ E^x_{0,n}\\ E^x_{m,0}\\ E^x_{m,n}\\ E^y_{m,n}\end{pmatrix} \tag{3.40}$$

and

$$\frac{\partial}{\partial z}\begin{pmatrix} E^x_{0,0}\\ E^x_{0,j}\\ E^x_{i,0}\\ E^x_{i,j}\\ E^y_{i,j}\end{pmatrix} = \begin{pmatrix} R^{x;y}_{0,0;0,0} & R^{x;y}_{0,0;0,n} & R^{x;y}_{0,0;m,0} & R^{x;x}_{0,0;m,n} & R^{x;y}_{0,0;m,n}\\ R^{x;y}_{0,j;0,0} & R^{x;y}_{0,j;0,n} & R^{x;y}_{0,j;m,0} & R^{x;x}_{0,j;m,n} & R^{x;y}_{0,j;m,n}\\ R^{x;y}_{i,0;0,0} & R^{x;y}_{i,0;0,n} & R^{x;y}_{i,0;m,0} & R^{x;x}_{i,0;m,n} & R^{x;y}_{i,0;m,n}\\ R^{x;y}_{i,j;0,0} & R^{x;y}_{i,j;0,n} & R^{x;y}_{i,j;m,0} & R^{x;x}_{i,j;m,n} & R^{x;y}_{i,j;m,n}\\ R^{y;y}_{i,j;0,0} & R^{y;y}_{i,j;0,n} & R^{y;y}_{i,j;m,0} & R^{y;x}_{i,j;m,n} & R^{y;y}_{i,j;m,n}\end{pmatrix} \times\begin{pmatrix} H^y_{0,0}\\ H^y_{0,n}\\ H^y_{m,0}\\ H^x_{m,n}\\ H^y_{m,n}\end{pmatrix}, \tag{3.41}$$

respectively. Here the indices run as $1\leqslant i\leqslant N_1$, $1\leqslant m\leqslant N_1$, $1\leqslant j\leqslant N_2$, and $1\leqslant n\leqslant N_2$. Each matrix element should also be understood as a block submatrix.

The other two symmetric modes are slightly different. For the even-odd mode, we find from Eq. (3.9)

$$E^y_{0,j}=E^x_{i,0}=0,\quad H^x_{0,j}=H^y_{i,0}=0.$$

With the total number of the excluded constant-zero variables being $(N_1+1)+(N_2+1)$, the truly independent unknown variables are left to a number of $M=\frac{1}{2}[(2N_1+1)(2N_2+1)+1]-1=\frac{1}{2}(N-1)$. The matrix elements that need to be removed in Q and R are now $Q^{y;y}_{0,j;0,n}$, $Q^{x;x}_{i,0;m,0}$, $R^{y;x}_{0,j;0,n}$, $R^{x;y}_{i,0;m,0}$, etc. Both matrices now have a contracted dimension of $M\times M$. In this case, Eqs. (3.30) and (3.32) have an explicit form of

$$\frac{\partial^2}{\partial z^2}\begin{pmatrix} E^x_{0,j}\\ E^y_{i,0}\\ E^x_{i,j}\\ E^y_{i,j}\end{pmatrix} = -\begin{pmatrix} Q^{x;x}_{0,j;0,n} & Q^{x;y}_{0,j;m,0} & Q^{x;x}_{0,j;m,n} & Q^{x;y}_{0,j;m,n}\\ Q^{y;x}_{i,0;0,n} & Q^{y;y}_{i,0;m,0} & Q^{y;x}_{i,0;m,n} & Q^{y;y}_{i,0;m,n}\\ Q^{x;x}_{i,j;0,n} & Q^{x;y}_{i,j;m,0} & Q^{x;x}_{i,j;m,n} & Q^{x;y}_{i,j;m,n}\\ Q^{y;x}_{i,j;0,n} & Q^{y;y}_{i,j;m,0} & Q^{y;x}_{i,j;m,n} & Q^{y;y}_{i,j;m,n}\end{pmatrix} \times\begin{pmatrix} E^x_{0,n}\\ E^y_{m,0}\\ E^x_{m,n}\\ E^y_{m,n}\end{pmatrix} \tag{3.42}$$

and

$$\frac{\partial}{\partial z}\begin{pmatrix} E^x_{0,j} \\ E^y_{i,0} \\ E^x_{i,j} \\ E^y_{i,j} \end{pmatrix} = \begin{pmatrix} R^{x;y}_{0,j;0,n} & R^{x;x}_{0,j;m,0} & R^{x;x}_{0,j;m,n} & R^{x;y}_{0,j;m,n} \\ R^{y;y}_{i,0;0,n} & R^{y;x}_{i,0;m,0} & R^{y;x}_{i,0;m,n} & R^{y;y}_{i,0;m,n} \\ R^{x;y}_{i,j;0,n} & R^{x;x}_{i,j;m,0} & R^{x;x}_{i,j;m,n} & R^{x;y}_{i,j;m,n} \\ R^{y;y}_{i,j;0,n} & R^{y;x}_{i,j;m,0} & R^{y;x}_{i,j;m,n} & R^{y;y}_{i,j;m,n} \end{pmatrix} \times \begin{pmatrix} H^y_{0,n} \\ H^x_{m,0} \\ H^x_{m,n} \\ H^y_{m,n} \end{pmatrix}, \tag{3.43}$$

respectively. Here the indices also run as $1 \leqslant i \leqslant N_1$, $1 \leqslant m \leqslant N_1$, $1 \leqslant j \leqslant N_2$, and $1 \leqslant n \leqslant N_2$. Each matrix element also represents a block submatrix.

For the odd-even mode, we find from Eq. (3.10)

$$E^x_{0,j} = E^y_{i,0} = 0, \quad H^y_{0,j} = H^x_{i,0} = 0.$$

The number of the truly independent unknown variables is also $M = \frac{1}{2}(N-1)$. The matrix elements that need to be removed in Q and R are now $Q^{x;x}_{0,j;0,n}$, $Q^{y;y}_{i,0;m,0}$, $R^{x;y}_{0,j;0,n}$, $R^{y;x}_{i,0;m,0}$, etc. Both Q and R are of dimension $M \times M$. We can write Eqs. (3.30) and (3.32) in an explicit form similar to Eqs. (3.42) and (3.43).

It can be easily checked that in every situation of the structural symmetry, the size of all reduced eigenproblems will add up to a number that is just the size of the original one without symmetry, which is $2N$. Therefore, no superfluous unphysical eigenmodes will be introduced when we solve these new symmetry-related size-reduced eigenproblems.

IV. CONSTRUCTION OF TRANSFER MATRIX UNDER MIRROR-REFLECTION SYMMETRIES

In the above section we have solved the EM fields within each slice of the waveguide structure using the basis of plane wave functions under mirror-reflection symmetries. To place the wave propagation problem in the framework of the TMM, we need to proceed to finish the construction of the transfer matrix for this grating slice. To do so, we need to write down the eigenfields existing in the two infinitely thin air films surrounding the slice, then use the boundary conditions of EM fields to find out the connection between the fields in these two air films, which according to definition is the transfer matrix under the adopted plane-wave basis.

The tangential components of the **E** and **H** fields in the left-hand side air film can be written into

$$E_{x(y)}(\mathbf{r}) = \sum_{ij} [E^+_{ij,x(y)} + E^-_{ij,x(y)}] e^{ik_{ij,x}x + ik_{ij,y}y}, \tag{4.1}$$

$$H_{x(y)}(\mathbf{r}) = \sum_{ij} [H^+_{ij,x(y)} + H^-_{ij,x(y)}] e^{ik_{ij,x}x + ik_{ij,y}y}. \tag{4.2}$$

The fields in the right-hand side air film can be obtained by simply replacing $E^{\pm}_{ij,x(y)}$ and $H^{\pm}_{ij,x(y)}$ with $U^{\pm}_{ij,x(y)}$ and $V^{\pm}_{ij,x(y)}$, respectively. There are definite analytical relations between the **H** and **E** fields,[27,28] which can be readily retrieved from the Maxwell's equation $\nabla \times \mathbf{E} = ik_0 \mathbf{H}$. The results can be written as $(H^+_{ij,x}, H^+_{ij,y})^T = T_{0,ij}(E^+_{ij,x}, E^+_{ij,y})^T$ and $(H^-_{ij,x}, H^-_{ij,y})^T = -T_{0,ij}(E^-_{ij,x}, E^-_{ij,y})^T$. The 2×2 matrix $T_{0,ij}$ has matrix elements $T^{11}_{0,ij} = -k_{ij,x}k_{ij,y}/(k_0\beta_{ij})$, $T^{12}_{0,ij} = (k^2_{ij,x} - k^2_0)/(k_0\beta_{ij})$, $T^{21}_{0,ij} = (k^2_0 - k^2_{ij,y})/(k_0\beta_{ij})$, and $T^{22}_{0,ij} = k_{ix}k_{ij,y}/(k_0\beta_{ij})$. β_{ij} is given by $\beta_{ij} = (k^2_0 - k^2_{ij,x} - k^2_{ij,y})^{1/2}$ for $k^2_0 - k^2_{ij,x} - k^2_{ij,y} \geqslant 0$, and $\beta_{ij} = i(k^2_{ij,x} + k^2_{ij,y} - k^2_0)^{1/2}$ for $k^2_0 - k^2_{ij,x} - k^2_{ij,y} < 0$.

Now suppose that we have obtained the EM fields within the i_{th} grating slice and in the two air films surrounding this grating slice, we can derive the transfer matrix for this slice. In the framework of the scattering-matrix (S-matrix) formulation,[23,24,28,33] we define column vectors $\Omega^{\pm}_{i-1} = (\ldots, E^{\pm}_{ij,x}, E^{\pm}_{ij,y}, \ldots)^T$, $\Omega^{\pm}_i = (\ldots, U^{\pm}_{ij,x}, U^{\pm}_{ij,y}, \ldots)^T$. Then the slice S matrix s^i is defined by

$$\begin{pmatrix} \Omega^+_i \\ \Omega^-_{i-1} \end{pmatrix} = s^i \begin{pmatrix} \Omega^+_{i-1} \\ \Omega^-_i \end{pmatrix} = \begin{pmatrix} s^i_{11} & s^i_{12} \\ s^i_{21} & s^i_{22} \end{pmatrix} \begin{pmatrix} \Omega^+_{i-1} \\ \Omega^-_i \end{pmatrix}. \tag{4.3}$$

For the sake of completeness and self-consistence, the procedure of solving this S matrix is briefly presented in Appendix A. More details can be referred to Ref. 28. It can be seen that the S matrix in Eq. (4.3) is of dimension $(4N) \times (4N)$.

Above we consider the transfer matrix for a general structure. In the case of mirror-reflection symmetries, we also need to place the eigenproblem for the two air films in the symmetry-reduced plane-wave space, following exactly the same procedure as we do to the grating slice. We should only pick up those truly independent unknown variables to solve the eigenproblem. For an air film, this procedure is quite simple, and can be analytically manipulated. The S matrix connecting these symmetry-reduced independent variables can also be calculated following the similar way as for a general structure,[28] as shown in Appendix A. Finally for the i_{th} grating slice we can write

$$\begin{pmatrix} \Omega^+_{M,i} \\ \Omega^-_{M,i-1} \end{pmatrix} = s^i_M \begin{pmatrix} \Omega^+_{M,i-1} \\ \Omega^-_{M,i} \end{pmatrix} = \begin{pmatrix} s^i_{M,11} & s^i_{M,12} \\ s^i_{M,21} & s^i_{M,22} \end{pmatrix} \begin{pmatrix} \Omega^+_{M,i-1} \\ \Omega^-_{M,i} \end{pmatrix}, \tag{4.4}$$

where $\Omega^{\pm}_{M,i-1}$ and $\Omega^{\pm}_{M,i}$ are column vectors comprising the independent variables of the plane-wave coefficients associated with a certain mirror-reflection symmetry, and s^i_M is the corresponding slice S matrix. For the x-axis or y-axis mirror-reflection symmetry, s^i_M has a dimension of $(2N) \times (2N)$. In the presence of the simultaneous x and y mirror-reflection symmetries, s^i_M is of dimension $(N+1) \times (N+1)$ for both the even-even and odd-odd modes, and of dimension $(N-1) \times (N-1)$ for both the even-odd and odd-even modes. Here we see that the size of the EM problem is reduced to one half for a photonic structure with either the x or the y mirror-reflection symmetry, and to about one quarter for a structure with simultaneous x and y mirror-reflection symmetries.

We notice here that the symmetry-reduced S matrix s_M attains all usual mathematical structures in connection with the usual matrix S. These include the important recursion

algorithm designed to calculate the overall S matrix for a slab from all the individual S matrices (such as s^i) for each composite slice,[23,24,33] as can be found in Appendix A. As is well known, one standard application of the TMM is to calculate the transmission and reflection spectra for the scattering of an incident EM wave by a grating slab. Another important application is to solve the photonic band structures for a photonic crystal grating structure. Since the S matrix stands on the basis of all these applications, we see that all usual theoretical and numerical techniques developed for a general structure can be directly used here for structures exhibiting mirror-reflection symmetries.

Up to now we only discuss the mirror-reflection symmetries existing in the lateral plane, namely, along the x and y directions. We find that they can reduce the number of the unknown variables used to represent the EM fields by twofold to fourfold, and consequently greatly release the burden of computer storage space and computational time. We will further show that if the structure has a mirror-reflection symmetry along the wave propagation direction, the z axis, the numerical burden can be further reduced to one half. To see this, we assume that a slab has a mirror-reflection symmetry with respect to the plane located at $z=0$. We designate the left and right half slabs as slab A and B, and the corresponding S matrix as S_A and S_B, respectively. Then for slab A we have

$$\begin{pmatrix} \Omega_1^+ \\ \Omega_0^- \end{pmatrix} = \begin{pmatrix} S_{11}^A & S_{12}^A \\ S_{21}^A & S_{22}^A \end{pmatrix} \begin{pmatrix} \Omega_0^+ \\ \Omega_1^- \end{pmatrix}, \tag{4.5}$$

where Ω_0^+ is assumed to be the incident field from the left-hand side of slab A. For slab B we have

$$\begin{pmatrix} \Phi_1^+ \\ \Phi_0^- \end{pmatrix} = \begin{pmatrix} S_{11}^B & S_{12}^B \\ S_{21}^B & S_{22}^B \end{pmatrix} \begin{pmatrix} \Phi_0^+ \\ \Phi_1^- \end{pmatrix}. \tag{4.6}$$

In Eq. (4.6), Φ_0^+ is assumed to be the incident field from the left-hand side of slab B. However, we can also assume that Φ_1^- is the incident field from the right-hand side of slab B. Since this incident wave will witness a structure exactly the same as slab A (due to the mirror-reflection symmetry), we can directly write down

$$\begin{pmatrix} \Phi_0^- \\ \Phi_1^+ \end{pmatrix} = \begin{pmatrix} S_{11}^A & S_{12}^A \\ S_{21}^A & S_{22}^A \end{pmatrix} \begin{pmatrix} \Phi_1^- \\ \Phi_0^+ \end{pmatrix}. \tag{4.7}$$

Comparing Eq. (4.6) and (4.7) we easily find the following symmetric relations between S_A and S_B:

$$S_{11}^B = S_{22}^A, \quad S_{22}^B = S_{11}^A,$$

$$S_{12}^B = S_{21}^A, \quad S_{21}^B = S_{12}^A. \tag{4.8}$$

These symmetric relations allows us to only calculate the S matrix for the first half of the considered slab, and thus reduce the numerical burden to one half of that without considering this z-axis mirror-reflection symmetry.

Similar arguments also apply to the whole slab. Due to the symmetry of the whole slab, a wave incident from the left-hand side and from the right-hand side will witness the same structure, so we have the same relations as Eq. (4.8), but now A and B denote the same identical slab. Let S be the S matrix for the whole slab, we have

$$S_{11} = S_{22}, \quad S_{12} = S_{21}, \tag{4.9}$$

which means that S is a block-symmetric matrix. As a result, we need only to numerically calculate two of the four block submatrices making up the overall S matrix, another relief of the numerical burden for the TMM. On the other hand, this z-axis symmetry can also find some applications in solution of the localized modes of the slab. The eigenmode can be classified into the even and odd modes, satisfying an eigenproblem half the size of the original one without symmetry consideration.

V. USAGE OF PERFECTLY MATCHED LAYERS TO ACCOUNT FOR ABSORBING BOUNDARY CONDITIONS

In the above discussion on wave propagation in PC waveguide structures, we assume that EM waves are perfectly confined in the waveguide channels, therefore, physically there should be no cross talk among different supercells. Numerically, the adoption of a sufficiently large supercell can guarantee negligible coupling between adjacent supercells and thus approach the ideal physical problem. However, in many cases, the confinement is not perfect, and the wave can leak out of the waveguide channel through the side wall during its propagation. For instance, the current best sample of 3D layer-by-layer photonic crystals working in the optical regime has a limited layer number (below 16 layers) along the (001) growth direction, and consequently a waveguide built in this platform will have a limited cladding layer number.[7,8] Therefore, the leakage of wave away from the waveguide channel is inevitable and cannot be neglected. Another example is the 2D PC slab waveguide. This waveguide relies on the 2D band gap to achieve the in-plane wave confinement, and on the index-guiding mechanism to realize the vertical wave confinement. Since the background photonic crystal does not have a complete 3D band gap, this type of waveguide is more vulnerable to defects than the above layer-by-layer PC waveguide. Roughness at the surface of the slab and at the side walls of the air holes etched into the slab as well as imperfect alignment of the lattice patterns can all induce scattering of wave off the waveguide, dominantly from the vertical direction.

This leakage will cause mutual coupling between adjacent supercells. Without taking this fact into full account, the TMM calculation results would be untrustful or even incorrect. To prevent this difficulty, the fields at the lateral boundaries of the supercell need to satisfy some absorbing boundary conditions, so that any wave impinging on the boundaries are completely absorbed and will not reach and disturb the adjacent supercell, and no reflection back from the boundaries occurs to disturb the studied system. One efficient way to achieve this goal is to place PMLs at the lateral boundaries of the supercell whenever physically there is leakage of wave through this boundary.

The PML is a kind of artificial anisotropic metallic and magnetic material which is specially designed for numerical

modeling of the absorbing boundary conditions. It is anisotropic in both the permittivity $\epsilon(\mathbf{r})$ and the permeability $\mu(\mathbf{r})$. For a general anisotropic material, ϵ and μ are both general second-order tensors (3×3 matrices). However, since the usual supercell adopted has a rectangular shape, and the boundaries are collinear to the x and y axes, it can be shown that the principal axes of the permittivity and permeability also are both coincident with the coordinate axes. Therefore, we can write $\hat{\epsilon}=(\epsilon_x,\epsilon_y,\epsilon_z)$ and $\hat{\mu}=(\mu_x,\mu_y,\mu_z)$. In this situation Maxwell's equations are

$$\nabla\times\mathbf{E}(\mathbf{r})=ik_0\hat{\mu}(\mathbf{r})\cdot\mathbf{H}(\mathbf{r}),\quad \nabla\times\mathbf{H}(\mathbf{r})=-ik_0\hat{\epsilon}(\mathbf{r})\cdot\mathbf{E}(\mathbf{r}). \tag{5.1}$$

$\hat{\epsilon}(\mathbf{r})$ and $\hat{\mu}(\mathbf{r})$ are both periodic functions in the lateral XY plane of the grating with the periods characterized by the supercell. Similar to the isotropic situation as discussed in Sec. II, we can derive from Eq. (5.1) the following four coupled equations satisfied by the tangential field components (E_x,E_y) and (H_x,H_y):

$$\frac{\partial}{\partial z}E_x=\frac{1}{-ik_0}\frac{\partial}{\partial x}\left[\frac{1}{\epsilon_z}\left(\frac{\partial}{\partial x}H_y-\frac{\partial}{\partial y}H_x\right)\right]+ik_0\mu_yH_y, \tag{5.2}$$

$$\frac{\partial}{\partial z}E_y=\frac{1}{-ik_0}\frac{\partial}{\partial y}\left[\frac{1}{\epsilon_z}\left(\frac{\partial}{\partial x}H_y-\frac{\partial}{\partial y}H_x\right)\right]-ik_0\mu_xH_x, \tag{5.3}$$

$$\frac{\partial}{\partial z}H_x=\frac{1}{ik_0}\frac{\partial}{\partial x}\left[\frac{1}{\mu_z}\left(\frac{\partial}{\partial x}E_y-\frac{\partial}{\partial y}E_x\right)\right]-ik_0\epsilon_yE_y, \tag{5.4}$$

$$\frac{\partial}{\partial z}H_y=\frac{1}{ik_0}\frac{\partial}{\partial y}\left[\frac{1}{\mu_z}\left(\frac{\partial}{\partial x}E_y-\frac{\partial}{\partial y}E_x\right)\right]+ik_0\epsilon_xE_x. \tag{5.5}$$

These equations can be solved in the plane-wave space in exactly the same way as the isotropic situation discussed in Sec. III, leading to the following coupled equations

$$\frac{\partial}{\partial z}E=T_1H,\quad \frac{\partial}{\partial z}H=T_2E, \tag{5.6}$$

where the matrices T_1 and T_2 have the same form as in Eqs. (3.12) and (3.13), except that the Fourier matrices of isotropic ϵ and μ should be replaced by the current anisotropic ones. In addition, the calculation of these matrices follow exactly the same Fourier expansion rules as in Eqs. (3.14)–(3.23). The matrices $[\epsilon_z]$ and $[\mu_z]$ are now

$$[\epsilon_z]_{ij;mn}=[\epsilon_z]_{i-m,j-n}=\frac{1}{d_1d_2}\int_{-d_1/2}^{d_1/2}\int_{-d_2/2}^{d_2/2}\epsilon_z(x,y)\times e^{-i(k_{ij,x}-k_{mn,x})x-i(k_{ij,y}-k_{mn,y})y}dxdy, \tag{5.7}$$

$$[\mu_z]_{ij;mn}=[\mu_z]_{i-m,j-n}=\frac{1}{d_1d_2}\int_{-d_1/2}^{d_1/2}\int_{-d_2/2}^{d_2/2}\mu_z(x,y)\times e^{-i(k_{ij,x}-k_{mn,x})x-i(k_{ij,y}-k_{mn,y})y}dxdy. \tag{5.8}$$

Other matrices $[\epsilon_x]$, $[\epsilon_y]$, $[\mu_x]$, and $[\mu_y]$ are also given by Eqs. (3.16)–(3.19), but the matrices within the integrand should be replaced by the anisotropic ones. Equations (3.20)–(3.23) are now given by

$$[1/\epsilon]_{j,n}(x)=\frac{1}{d_2}\int_{-d_2/2}^{d_2/2}\left[\frac{1}{\epsilon_y(x,y)}\right]e^{-i(k_{ij,y}-k_{mn,y})y}dy, \tag{5.9}$$

$$[1/\epsilon]_{i,m}(y)=\frac{1}{d_1}\int_{-d_1/2}^{d_1/2}\left[\frac{1}{\epsilon_x(x,y)}\right]e^{-i(k_{ij,x}-k_{mn,x})x}dx, \tag{5.10}$$

$$[1/\mu]_{j,n}(x)=\frac{1}{d_2}\int_{-d_2/2}^{d_2/2}\left[\frac{1}{\mu_y(x,y)}\right]e^{-i(k_{ij,y}-k_{mn,y})y}dy, \tag{5.11}$$

$$[1/\mu]_{i,m}(y)=\frac{1}{d_1}\int_{-d_1/2}^{d_1/2}\left[\frac{1}{\mu_x(x,y)}\right]e^{-i(k_{ij,x}-k_{mn,x})x}dx. \tag{5.12}$$

The remaining procedure to construct the transfer matrix for an individual grating slice under different situations of structural symmetry follows the same way developed in Sec. III, as all informations of the photonic structure have been essentially involved in the matrices T_1, T_2, and $P=-T_1T_2$. As is well known, the standard application of the TMM to a photonic crystal includes solution of the transmission and reflection spectra, and the photonic band structures. Appendix B briefly describes how to solve the photonic band structures (or dispersions) for lossless and lossy modes on the basis of the S matrix for the unit cell of the photonic crystal. These standard applications are not affected by the introduction of PML's into the photonic structure, because all information about the PML's has been involved in the S matrix itself. Instead, the usage of PML's can handle the leakage problem commonly encountered in the solution of wave propagation in integrated optical elements by means of the TMM. For instance, it is possible to quantitatively account for the propagation loss of EM waves due to imperfect confinement of EM waves within the waveguide channel. Conventionally, this problem is attacked by means of the FDTD technique. As we have noted in the Sec. I, for a very long waveguide, the FDTD simulation is not as numerically economic as the TMM.

VI. LOCALIZED MODES IN 2D PC SLAB AND SLAB WAVEGUIDE STRUCTURES

As we have noted in Sec. I, 2D PC slab waveguides are popular because of their ease of fabrication in the infrared wavelength. The schematic configuration of a typical 2D PC slab waveguide is shown in Figs. 1(c) and 1(d). The background 2D PC is made from a triangular lattice of air holes etched into a dielectric slab suspended in air, the so-called air-bridge structure, as shown in Fig. 1(b). By leaving one row of holes unetched along the ΓJ direction, a waveguide is formed. The lateral optical confinement is supported by the in-plane (the XZ plane) band gap for the 2D PC, while the

vertical confinement (along the *y* direction) is provided by the index-guiding mechanism for the high-dielectric planar slab.

The band diagrams of the localized modes in the PC slab and the guided modes in the waveguide have been investigated extensively by means of the PWM and the FDTD technique. In the PWM simulation, a supercell technique is used and the periodic boundary conditions are adopted in both the *x* and *y* directions.[13] Because the PML is not inserted into the boundary of the supercell, the coupling between adjacent supercells is not screened. However, this cross-talk will not affect those truly localized modes, since their exponentially decaying field tail automatically approaches zero at the boundary of a large enough supercell. In the FDTD simulation,[14] the periodic boundary condition is used in the *x* direction, while the absorbing boundary condition is imposed in the *y* direction. In our TMM simulation, we also utilize a supercell. The periodic boundary condition is always used in the *x* direction because of the perfect in-plane confinement. In the *y* direction, both the periodic boundary condition and the absorbing boundary condition are tried. We notice that there are two folds of mirror-reflection symmetries for both the bare PC slab and the PC slab waveguide structures when we choose appropriate unit cell and supercell configurations, as shown in Figs. 1(b)–1(d). Therefore, the problem can be reduced into four smaller ones for eigenmode with the even-even, odd-odd, even-odd, and odd-even symmetries, respectively, as has been described in Secs. II and III.

Let us first look at the localized modes supported by the bare 2D PC slab. The standard band diagram for a triangular lattice is plotted along the high-symmetry lines Γ-*X*-*J*-Γ in the first Brillouin zone, whose configuration is shown in Fig. 1(a). Due to the symmetry of the lattice, the line *J*-*X* is equivalent to the line J'-X'. This symmetry allows us to calculate the whole band diagrams along only two crystalline directions, the ΓJ and ΓX directions. As displayed in Fig. 1(b), the unit cell in both directions has mirror-reflection symmetries along the *x*, *y*, and *z* directions, so that the numerical burden of the TMM calculation can be reduced as much as possible.

To make convenient comparisons with other theoretical methods, we consider a structure that has been investigated in Ref. 13 by using the PWM. The PC slab has a large radius of air holes $r=0.45a$, a thickness $w=0.6a$, and a dielectric constant $\epsilon=12$. Here *a* is the lattice constant of the triangular lattice. In our TMM simulation, the primitive unit cell is always used to achieve optimum numerical convergence. Along the ΓJ direction, the adopted unit cell has a size $\sqrt{3}a\times 5.4a\times 0.5a$, and the two primitive-lattice basis vectors in the *XY* plane are $\mathbf{a}_1=(\sqrt{3}a,0,0)$ and $\mathbf{a}_2=(0,5.4a,0)$. The third basis vector for the 3D lattice is $\mathbf{a}_3=[(\sqrt{3}/2)a,0,0.5a]$, reflecting the symmetry of the triangular lattice. Similarly, along the ΓX direction, the unit cell is of size $a\times 5.4a\times(\sqrt{3}/2)a$, and the two primitive-lattice basis vectors in the *XY* plane are $\mathbf{a}_1=(a,0,0)$ and $\mathbf{a}_2=(0,5.4a,0)$, and the third basis vector is $\mathbf{a}_3=(0.5a,0,(\sqrt{3}/2)a)$. Because the primitive unit cell is not arrayed in an orthogonal lattice, a phase shift at the right-hand side of the unit cell must be taken into account in solution of the photonic band structures.[28,33]

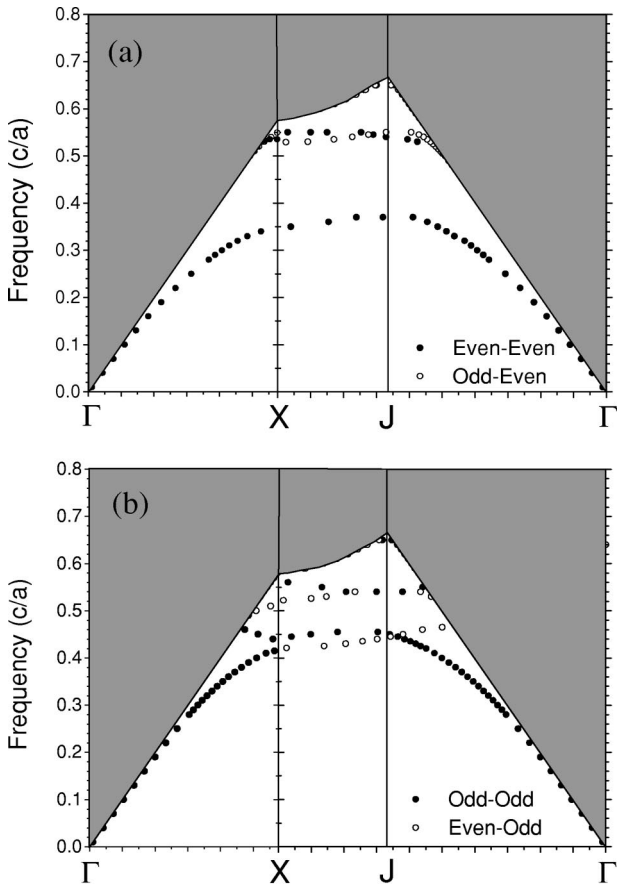

FIG. 2. Calculated band diagrams for the localized modes supported in a 2D PC slab made from etching a triangular lattice of air holes (with a radius $r=0.45a$) into a dielectric planar slab with a thickness $w=0.6a$ and a dielectric constant $\epsilon=12$. (a) TE-like localized modes; (b) TM-like localized modes. No PML's are placed at the boundary of the supercell in the TMM calculations.

As has been noted above, the absorption boundary condition in the *y* direction is not indispensable for the truly localized modes. To see this, we first consider a situation where the PML's are not placed at the *y*-axis boundary of the supercell. The calculation results are shown in Fig. 2(a) for the even-even and odd-even modes, and in Fig. 2(b) for the odd-odd and even-odd modes, respectively. Only those truly localized modes are displayed, while many other nonlocalized modes (or leaky modes) have been shadowed in the gray region with the light cone lying at the boundaries. In our simulation, up to 11×31 and 9×31 plane waves have been adopted to expand the EM fields in the *XY* plane for the ΓJ and ΓX directions, respectively. Notice that for clarity, here and throughout all the rest of this paper, all plane-wave numbers are referred to the uncontracted plane-wave space without any symmetry consideration. Because all symmetric modes are defined with respect to the E_x field, we see that the former two modes have dominant E_x and H_y fields, and correspond to the so-called TE-like modes, while the latter two modes have dominant E_y and H_x fields, and thus correspond to the so-called TM-like modes in literatures.[13–18] It

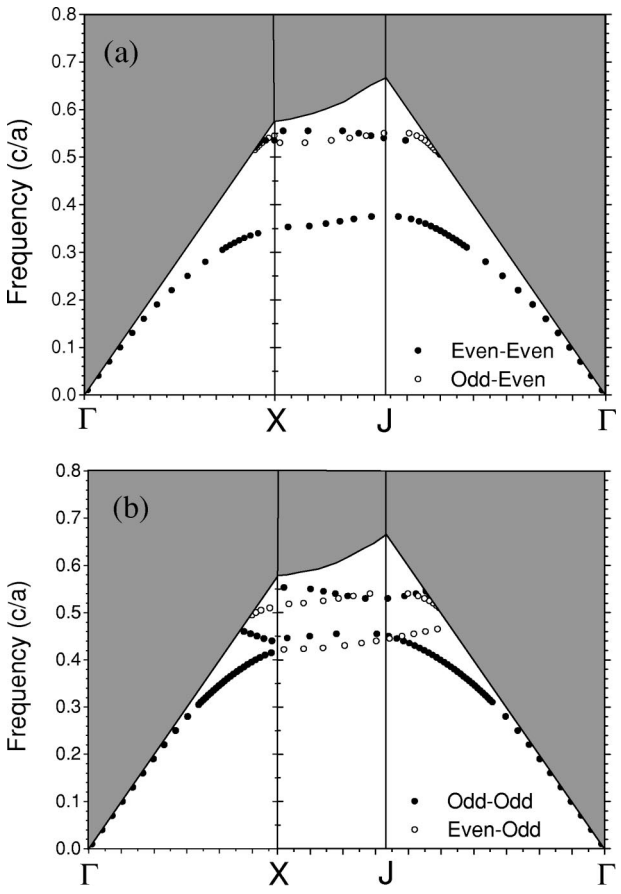

FIG. 3. Same as Fig. 2, except that the PML's are placed at the boundary of the supercell in the TMM calculations.

can be found that there is a wide band gap for the TE-like localized modes at frequencies $0.375-0.500(c/a)$, while there is only very weak band gap centered around $0.470(c/a)$ for the TM-like localized modes. This is consistent with the fact that for a pure 2D photonic crystal made from high filling-fraction air holes, the TE-mode band gap is far wider than the TM-mode band gap. The calculation results of the band diagrams overall are in agreement with those reported in Ref. 13, where the band gap for the TE-like localized modes lies at frequencies $0.355-0.500(c/a)$. There is slight discrepancy on the lower bandgap edge position for the two calculations, and this may be induced by different convergence behaviors of the TMM and the PWM.

Next we place two identical PML slabs at the *y*-axis boundary of the supercell. Each PML slab is $0.3a$ thick in each supercell (and totally $0.6a$ thick), and the permittivity and permeability are chosen as $\epsilon_x=\epsilon_z=\alpha$, $\epsilon_y=1/\alpha$, $\mu_x=\mu_z=\alpha$, $\mu_y=1/\alpha$, where α is set to be $3+3i$. The supercell size is the same as in Fig. 2. The calculation results of the band diagrams are shown in Figs. 3(a) and 3(b) for the TE-like and TM-like localized modes. Other modes originally appearing in Figs. 2(a) and 2(b) above the light cone turn out to have non-negligible imaginary part in the Bloch's wave vector k_z and therefore they are nonpropagation decay modes along the *z* direction, or equivalently, leaky modes for the PC slab along the vertical *y* direction. It is found that the imaginary part for those strongly localized modes (far away from the light cones) can reach a number as tiny as below $10^{-5}(\pi/a)$, and thus is completely negligible. The overall band diagrams are in good agreement with Figs. 2(a) and 2(b). This indicates that the absorbing boundary condition indeed is not indispensable for solution of the optical properties of the truly localized modes in the 2D PC slab.

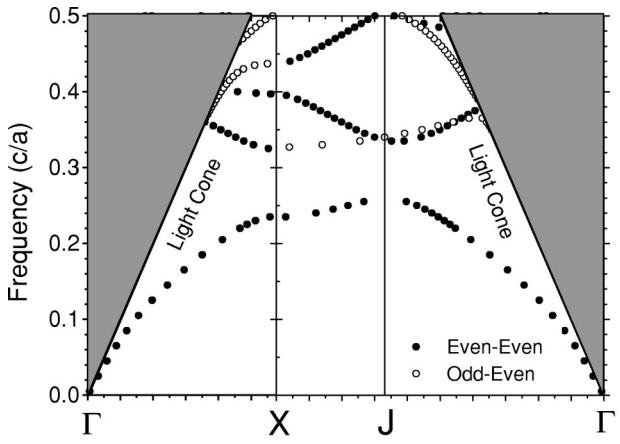

FIG. 4. Calculated band diagrams for the TE-like localized modes supported in a 2D PC slab made from etching a triangular lattice of air holes into a dielectric planar slab. The structure has parameters of $r=0.29a$, $w=0.6a$, and $\epsilon=11.56$. No PML's are placed at the boundary of the supercell in the TMM calculations.

The above structure has too large air holes and too thin dielectric veins between the air holes, and thus is not experimentally preferable even if it has a large band gap. To ease fabrication effort using lithographic techniques, the radius of the air holes need to be reduced in the compromise of the bandgap size. To this end, we consider another structure with $r=0.29a$, $w=0.6a$, and $\epsilon=11.56$. This structure has been investigated in Ref. 14 by means of the FDTD technique. Since the band gap only exists for the TE-like localized modes, we confine our computation to this polarization mode. In our calculation, we have adopted the same supercell as for the PC structure shown in Figs. 2 and 3. In addition, we also consider both situations with or without the PMLs placed at the *y*-axis boundary of the supercell. The calculated band diagrams of the localized modes are displayed in Figs. 4 and 5, respectively. Good agreement can also be found between the two calculation results. The band gap lies at frequencies $0.259-0.326(c/a)$. As a comparison, Ref. 14 reports a FDTD calculation result of the band gap as lying at frequencies $0.256-0.320(c/a)$, slightly downshift compared to our TMM simulation result.

Now we proceed to look at a waveguide brought into this 2D PC slab background by leaving one row of air holes unetched along the ΓJ direction. To solve the guided mode within the band gap, we use a supercell of size $5\sqrt{3}a \times 5.4a \times a$, which possesses mirror-reflection symmetries along all the *x*, *y*, and *z* directions, and the PML's are not used. Up to 33×27 plane waves have been adopted in the TMM solution of the band diagrams of the guided modes. The results are displayed in Fig. 6. There are two guided-mode bands with different symmetries. The lower band has an even-even mirror-reflection symmetry, and spans from the

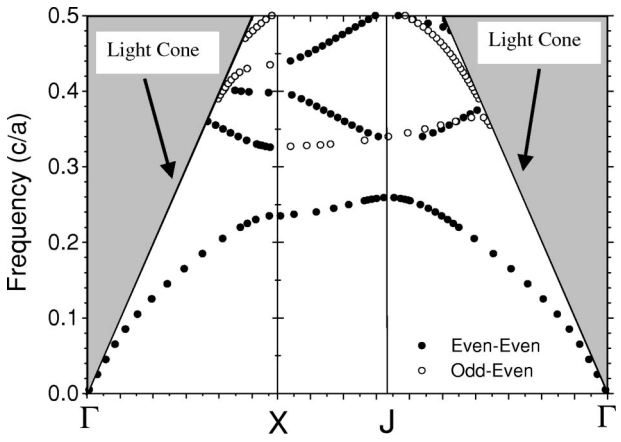

FIG. 5. Same as Fig. 4, except that the PML's are placed at the boundary of the supercell in the TMM calculations.

frequency $0.264(c/a)$ to the frequency $0.280(c/a)$. The higher band has an odd-even mirror-reflection symmetry, and spans from $0.286(c/a)$ to $0.297(c/a)$. Since the two bands do not cross over in frequency, we see that this waveguide supports single-mode operation of the localized guided mode. We have also performed TMM simulations for the situation of using the PML's, and obtained almost the same guided-mode band diagrams. The overall characteristic of the guided-mode diagrams calculated by the TMM is in accordance with those reported in Ref. 14, except for some discrepancies in the absolute position of the guided-mode bands. In Ref. 14, the first guided-mode band extends from $0.271(c/a)$ to $0.280(c/a)$, and the second band spans from $0.28(c/a)$ to $0.291(c/a)$. Experimental investigations have been reported on this waveguide structure, and it is found that EM waves excited at frequency $0.2686(c/a)$ can freely propagate along the waveguide, and thus correspond to a guided mode.[37] A quick glance at the theoretical and experimental results immediately shows that our TMM simulation has achieved better agreement with experiment than the FDTD technique. This is a convincing support of the efficiency and accuracy of the proposed TMM.

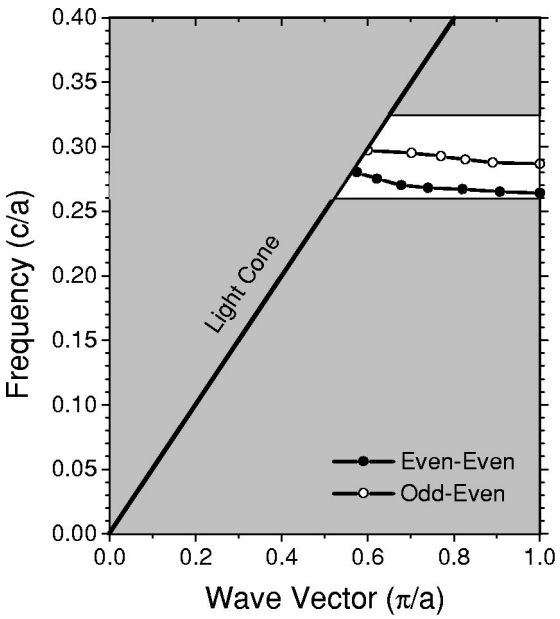

FIG. 6. Calculated band diagrams for the TE-like guided modes supported in a waveguide built in the 2D PC slab structure shown in Fig. 4 along the ΓJ direction.

VII. GUIDED MODES IN 3D LAYER-BY-LAYER PC WAVEGUIDES

We turn to another important kind of 3D PC waveguide structures, waveguides created in a 3D layer-by-layer photonic crystal by removing a single rod from an otherwise perfect lattice, which we call the missing-rod waveguides. This kind of structures has been extensively investigated both theoretically and experimentally[5–12] as the existence of a complete band gap in the background crystal may supply a possibility to realize 3D optical confinement in the waveguide.

Figures 7(a) and 7(b) demonstrate the top-view and side-view configuration of the 3D waveguide. The coordinate is chosen so that the waveguide axis is parallel to the *z* axis, and the *y* axis is collinear with the (001) growth direction of the crystal. The crystal is formed by stacking rectangular dielectric rods in a woodpile fashion. Each rod has width and thickness of *w* and *h*, respectively. A mirror-reflection symmetry with respect to the *x* axis can be found in the structure. Therefore, the guided mode supported in this waveguide can be classified into the even and odd modes with respect to the mirror-reflection plane *YZ*. This structural symmetry has been employed in the recent investigation by means of the conventional PWM.[11] However, the symmetric relations there between plane-wave coefficients appear more complicated and less clarified compared to those found in the current TMM formulation. The reason is that the field component under study in the TMM (E_x here) is naturally collinear with the symmetric axis, while in the conventional PWM, every plane-wave coefficient involves three components (E_x,E_y, and E_z) of the fields. On the other hand, recent study has shown that the TMM can exhibit much faster numerical convergence than the conventional PWM in solution of the photonic band gaps for this particular layer-by-layer photonic crystal structure.[28] Therefore, it can be expected that the TMM can also yield better accuracy in study of the current waveguide structure.

Let us first look at two waveguide structures that were investigated previously using either the conventional PWM or the FDTD technique. In the first structure, the dielectric rod has a width of $w=0.25a$, thickness of $h=0.3125a$, and a dielectric constant of $\epsilon=11.56$. Here a is the lattice constant of the crystal, which is just the center-to-center distance of the adjacent rods in each layer. In Ref. 11, the PWM calculation shows that a complete band gap opens at frequency $0.366-0.434(c/a)$ for the photonic crystal, and two guided-mode bands exist in the waveguide. The cutoff frequency of the lower band lies at the frequency $0.375(c/a)$. Due to the cross over of the upper band in frequency, the waveguide overall does not support single-mode operation. In Ref. 11, both the photonic crystal and the waveguide are

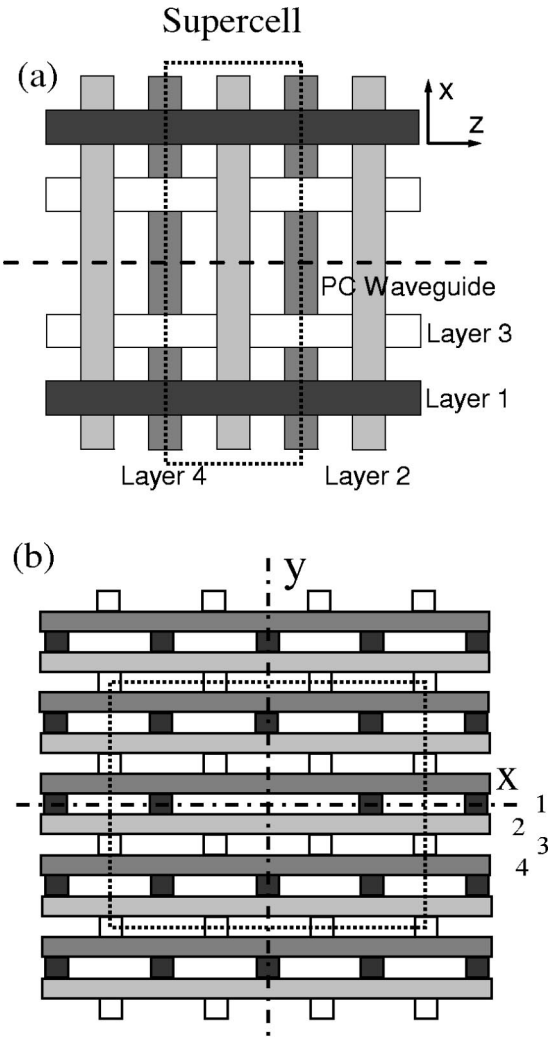

FIG. 7. (a) Top-view and (b) side-view schematic configuration of a 3D layer-by-layer PC waveguide structure and the symmetric supercell used in solution of the band diagrams of the guided modes. The crystal is made by stacking rectangular dielectric rods in a woodpile fashion.

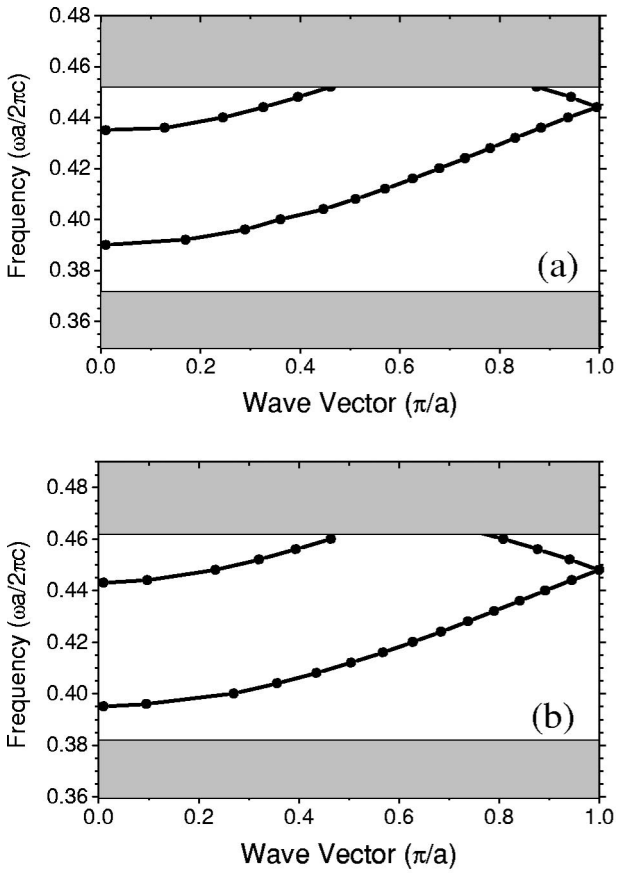

FIG. 8. Calculated band diagrams of the guided modes supported in the 3D layer-by-layer PC waveguide shown in Fig. 7. (a) The rod has width $w=0.25a$, thickness $h=0.3125a$, and a dielectric constant $\epsilon=11.56$. (b) The rod has parameters of $w=0.25a$, $h=0.3a$, and $\epsilon=11.56$.

solved using the same supercell technique in order to obtain consistent result of the guided-mode band in reference to the complete band gap for the background crystal. A supercell of size $5a\times 20h\times a$ and up to 6500 plane waves have been used there. Later more deliberate comparison study by means of the PWM and the TMM as reported in Ref. 28 has adopted the primitive unit cell of the crystal, and therefore has obtained much better accuracy in determining the band gap positions. The PWM calculation using $13\times 13\times 13$ plane waves finds a PBG located at $0.372-0.445(c/a)$, while the TMM calculation using 11×11 plane waves yields a PBG lying at $0.376-0.452(c/a)$. It is found that the TMM exhibits a much better numerical convergence behavior than the PWM. So we will choose the TMM result as the standard reference for the following waveguide study. We have revisited the waveguide structure using the TMM under the *x*-axis mirror-reflection symmetry. In our calculation, we adopt a $5a\times 20h\times a$ supercell centered around the waveguide axis, periodic boundary conditions in both directions of the *XY* plane, and up to 29×29 plane waves. The result is shown in Fig. 8(a). The two-band guided-mode characteristic and multimode behavior can be clearly seen. It is found that all guided modes have an odd mirror-reflection symmetry with respect to the *x* axis, and the corresponding **E** field is dominantly (but not purely) polarized along the *y* axis, the (001) growth direction of the crystal. No even guided modes are supported in the waveguide. The cutoff frequency of the waveguide lies at $0.390(c/a)$, in some distance from the lower bandgap edge of the background crystal. The overall features of the calculated band diagrams are in consistence with the results reported in Ref. 11. However, there is an overall upshift of the guided-mode bands together with the band gap for the crystal from the PWM calculation results in Ref. 11. This reflects the fact that the conventional PWM has a comparatively slower convergency.

The second waveguide structure has slightly geometrical parameters, where $w=0.25a$, $h=0.30a$, and $\epsilon=11.56$. This structure has been studied in Ref. 9 by means of both the PWM and FDTD technique. The TMM calculation result of the guided-mode band diagram is shown in Fig. 8(b). The overall characteristic of the two-band diagram and multimode behavior is similar to that in Fig. 8(a). The PBG of the background crystal is located at $0.382-0.462(c/a)$, as is

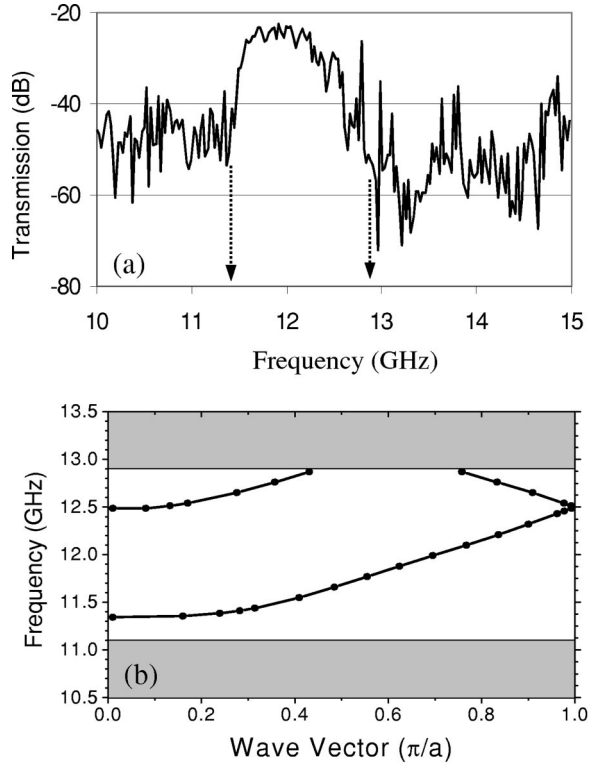

FIG. 9. (a) Experimental transmission spectrum and (b) calculated band diagrams of the guided modes for a microwave 3D layer-by-layer PC waveguide shown in Fig. 7. The crystal is made from alumina rods, and has parameters of $a=10.9$ mm, $w=3.2$ mm, $h=3.2$ mm, and $\epsilon=9$.

shown by the two gray domains in Fig. 8(b). The waveguide cutoff frequency is $0.395(c/a)$. As a comparison, in Ref. 9, the PWM calculation reports a PBG lying at $0.380-0.444(c/a)$, and the FDTD simulation reports a two-band diagram while single-mode behavior for the waveguide. The lower guided-mode band spans from the cutoff frequency at $0.392(c/a)$ to $0.440(c/a)$, and this result is close to our TMM calculations. The qualitative discrepancy in regard to the single-mode or multimode feature might be explained by the too lower upper bandgap edge set in Ref. 9, which renders the behavior of the higher guided-mode band in the frequency range between $0.444(c/a)$ and $0.462(c/a)$ indiscernible.

Above we only compare theoretical results obtained by using different numerical approaches. To attain more confidence, it is also important to compare with the experimental measurement. Recently, Sell *et al.* built a microwave 3D layer-by-layer photonic crystal by using alumina rods and measured the response of the missing-rod waveguide to the input microwave signal from a monopole probe.[12] The crystal has parameters of $a=10.9$ mm, $w=3.2$ mm, $h=3.2$ mm, and $\epsilon=9.0$. The TMM calculation shows a complete PBG lying between 11.14 and 12.92 GHz. A typical measurement result of the transmission spectrum is displayed in Fig. 9(a). As the waveguide is excited by a localized source, the radiation will dissipate in all directions at frequencies beyond the band gap, and only a small fraction of energy can reach the receive probe, resulting in a low level in the transmission spectrum. A high-level transmission band located between about 11.4 and 12.9 GHz can be found in Fig. 9(a), and this corresponds to the guided-mode band of the waveguide. We have carried out TMM calculations on this waveguide, and the band diagrams are shown in Fig. 9(b). The waveguide cutoff frequency is 11.35 GHz, and the guided-mode band extends into the upper bandgap edge of the crystal. In Fig. 9(a) one can find a dip in the high-transmission band around 12.6 GHz, this might correspond to the crossover region of the lower and higher guided-mode bands in Fig. 9(b), which is centered at about 12.5 GHz. The overall agreement between theory and experiment is good. This indicates that the TMM can effectively handle the wave propagation problem in 3D PC waveguides. As a comparison, our PWM calculation using 6500 plane waves has yielded a lower cutoff frequency at about 11.14 GHz, in far worse agreement with the experimental observations than the TMM calculations.

VIII. SYMMETRY CONSIDERATION OF COUPLING BETWEEN PC WAVEGUIDES AND EXTERNAL WAVEGUIDES

In the above sections, we have systematically discussed how the structural symmetries involved in a 3D PC waveguide can be used in solution of Maxwell's equations in the framework of the TMM. The field symmetry associated with a particular guided mode can be discerned and classified. This classification can prove helpful for understanding the coupling of the PC waveguide with external input/output signal channels.

Let us first suppose that the input source is a plane wave propagating in free space and collimated with the waveguide axis and that the PC waveguide possesses two-fold mirror-reflection symmetries. The polarization of the plane wave will determine what symmetric mode can be excited in the waveguide. According to the analysis made in Secs. III and IV [for instance, see Eqs. (3.7)–(3.10)], an *x*-axis polarized plane wave has an even-even symmetry, because the only field components are E_x, and H_y. So this pane wave can only excite the even-even symmetrical mode in the PC waveguide. For the same reason, an *y*-axis polarized plane wave can only excite an odd-odd mode in the waveguide. Other linear polarization states can be decomposed into linear superposition of the two polarization states, and thus can excite both the even-even and odd-odd modes in the waveguides. For more complex field profile of the incident wave, such as a Gaussian beam, the incident signals usually possess a rotational symmetry. Therefore, they can also be decomposed into linear superposition of the four symmetric modes, and coupled into the waveguide. The excitation power for each mode can be calculated separately in their own plane-wave sub-space because they will not interact with each other.

For waveguides working in the infrared wavelength, such as the 2D PC slab waveguides, a more realistic coupling fashion is connecting the PC waveguide with external conventional dielectric wire waveguides.[15,16,34,35] A plane-wave incidence proves to be too low-efficient in coupling. As the wire waveguide has a rectangular shape, and is collimated

with the PC waveguide axis, it possesses the same mirror-reflection symmetries as the PC waveguide. For an air-bridge system, the wire waveguide can also support the even-even, odd-odd, even-odd, and odd-even symmetric guided modes, whose dispersions can be solved numerically in the same TMM framework as for the 2D PC slab waveguide. In this way, one can selectively excite different symmetric modes in the PC waveguide by injecting signal into the wire waveguide with a particular symmetry. Therefore, even for a PC waveguide supporting multimodes but each mode with different symmetries, one can still pick up a particular symmetric mode and the waveguide appears as if working in the single-mode fashion.

IX. SUMMARIES AND CONCLUSIONS

In summary, we have systematically explored the application of structural symmetries associated with 3D PC waveguide structures to solve EM wave propagation in these waveguides in the framework of the plane-wave-based TMM. Optimal Fourier expansion rules on the EM fields and the material permittivity and permeability functions have been fully exploited in order to achieve fast numerical convergency in these 3D TMM simulations. Starting from Maxwell's equations, the symmetry of the EM fields in the real space and plane-wave space is revealed under various mirror-reflection symmetries. These symmetric relations can be used to significantly reduce the requirement on the computer memory space and the computation time, and greatly release the numerical burden that are involved in the plane-wave-based TMM for the solution of guided modes supported in the 3D PC waveguides. The solution to the EM problems under these mirror-reflection symmetries in both the real space and the plane-wave space has been discussed in a systematic way and in great detail. In addition, the classification of symmetry in the guided modes will help people to understand the coupling of the PC waveguides with external input/output channels such as dielectric slab or wire waveguides, which usually possess the same structural symmetries as the PC waveguides.

We have used the symmetry-enhanced TMM to handle two important kinds of 3D PC waveguide structures, the 3D layer-by-layer PC waveguides and 2D PC slab waveguides. The supercell technique and associated periodic boundary conditions are used to model wave propagation in the PC waveguide system with complete optical confinement. The absorbing boundary condition is also employed to solve localized modes supported by the bare 2D PC slab and guided modes in the slab waveguides by placing PML's at the off-plane boundary of the supercell. We have compared the TMM calculation results of the band diagrams for the localized modes and guided modes to other calculation results reported in previous literatures using the PWM and the FDTD technique. The agreement in the overall features of the band diagrams is satisfactory. We have also compared the TMM simulation results with the experimental measurements on an infrared 2D PC slab waveguide and a microwave 3D layer-by-layer PC waveguide, and better agreement is achieved in comparison with other theoretical investigation results. This indicates that the symmetry-enhanced TMM can effectively, economically, and accurately explore the optical properties of waveguide structures built in 3D photonic crystal structures, and therefore can find its application in understanding EM wave propagation in various functional elements embedded in the background of the inhomogeneous photonic crystal media.

ACKNOWLEDGMENTS

Ames Laboratory is operated for the U.S. Department of Energy (DOE) by Iowa State University under Contract No. W-7405-Eng-82.

APPENDIX A: CONSTRUCTION OF *S* MATRIX FOR A UNIT CELL OF A PHOTONIC CRYSTAL

When one applies the TMM to a photonic crystal, the unit cell of the photonic crystal usually is divided into a number of thin slices, each of which can be approximated as a lamellar grating. We first solve the *S* matrix connecting the plane-wave coefficients in the two hand sides of each slice, then construct the overall *S* matrix for the whole unit cell by means of a recursion algorithm.

The slice *S* matrix depends only on the eigenmodes within the lamellar grating, which satisfy Eqs. (3.11) and (3.26) in the plane-wave space. Let us consider the i_{th} slice (lying between $z=z_{i-1}$ and $z=z_i$) in a general photonic structure. Solution of Eq. (3.26) will yield $2N$ (with N being the used plane-wave number) eigenvalues [denoted as $\beta_i^2, i=1,2,\ldots,2N$, with $\mathrm{Im}(\beta_i)\geqslant 0$] of the matrix P. In addition, the $(2N)\times(2N)$ matrix S_a, whose j_{th} column is the eigenvector corresponding to the eigenvalue β_j^2, can also be obtained simultaneously. The eigenmode corresponding to β_i^2 is $E_i'(z)=E_{a,i}^+(z)+E_{a,i}^-(z)$, $E_{a,i}^+(z)=E_i^+ e^{i\beta_i(z-z_{i-1})}$, $E_{a,i}^-(z)=E_i^- e^{-i\beta_i(z-z_{i-1})}$, where E_i^+ and E_i^- are both unknown variables. Further define column vector $\beta=(\ldots,\beta_i,\ldots)^T$, $E_a^+=[\ldots,E_{a,i}^+(z),\ldots]^T$ and $E_a^-=[\ldots,E_{a,i}^-(z),\ldots]^T$. The electric field column vector E are now expressed into the superposition of all the eigenmodes $E=S_a(E_a^+ + E_a^-)$. The corresponding magnetic field column vector are obtained from Eq. (3.11) and reads $H=T_1^{-1}\partial/\partial z\, E = T_1^{-1}S_a\,\partial/\partial z\,(E_a^+ + E_a^-) = iT_1^{-1}S_a\beta\,(E_a^+ - E_a^-) = T_a(E_a^+ - E_a^-)$, where $T_a = iT_1^{-1}S_a\beta$. It proves convenient to write down the electric and magnetic fields at an arbitrary point inside the grating slice into a concise form

$$\begin{pmatrix} E(z) \\ H(z) \end{pmatrix} = \begin{pmatrix} S_a & S_a \\ T_a & -T_a \end{pmatrix} \begin{pmatrix} E_a^+(z) \\ E_a^-(z) \end{pmatrix}. \tag{A1}$$

The EM fields in the two air films around the grating slice can also be solved in the same way, and the results have been expressed in Eqs. (4.1) and (4.2), but we can rewrite them in a way similar to Eq. (A1). Match of boundary conditions requests all tangential field components of each plane wave be continuous at the two interfaces between the air films and the grating slice. At the left interface $z=z_{i-1}$

$$\begin{pmatrix} S_0 & S_0 \\ T_0 & -T_0 \end{pmatrix}\begin{pmatrix} \Omega_{i-1}^{+} \\ \Omega_{i-1}^{-} \end{pmatrix}=\begin{pmatrix} S_a & S_a \\ T_a & -T_a \end{pmatrix}\begin{pmatrix} E_a^{+}(z_{i-1}) \\ E_a^{-}(z_{i-1}) \end{pmatrix}, \quad \text{(A2)}$$

while at the right interface $z=z_i$

$$\begin{pmatrix} S_0 & S_0 \\ T_0 & -T_0 \end{pmatrix}\begin{pmatrix} \Omega_{i}^{+} \\ \Omega_{i}^{-} \end{pmatrix}=\begin{pmatrix} S_a & S_a \\ T_a & -T_a \end{pmatrix}\begin{pmatrix} E_a^{+}(z_{i}) \\ E_a^{-}(z_{i}) \end{pmatrix}, \quad \text{(A3)}$$

where S_0 and T_0 are counterparts of S_a and T_a in an air film. S_0 is a unit matrix, while T_0 is a block-diagonal matrix each block of which is a 2×2 matrix already given by $T_{0,ij}$ below Eq. (4.2). Within the grating slice we have

$$\begin{pmatrix} E_a^{+}(z_i) \\ E_a^{-}(z_i) \end{pmatrix}=\begin{pmatrix} e^{i\beta h} & 0 \\ 0 & e^{-i\beta h} \end{pmatrix}\begin{pmatrix} E_a^{+}(z_{i-1}) \\ E_a^{-}(z_{i-1}) \end{pmatrix}, \quad \text{(A4)}$$

where $h=z_i-z_{i-1}$ is the thickness of the slice, $e^{i\beta h}$ denotes a $(2N)\times(2N)$ diagonal matrix whose element is $e^{i\beta_i h}, i=1,2,\ldots,2N_0$. Deleting $[E_a^{+}(z_{i-1}),E_a^{-}(z_{i-1})]^T$ and $[E_a^{+}(z_i),E_a^{-}(z_i)]^T$ from Eqs. (A2)–(A4) and making some analytical derivations yields

$$\begin{pmatrix} \Omega_{i}^{+} \\ \Omega_{i}^{-} \end{pmatrix}=\begin{pmatrix} a_{11} & a_{12} \\ a_{21} & a_{22} \end{pmatrix}^{-1}\begin{pmatrix} e^{i\beta h} & 0 \\ 0 & e^{-i\beta h} \end{pmatrix}\begin{pmatrix} a_{11} & a_{12} \\ a_{21} & a_{22} \end{pmatrix}\begin{pmatrix} \Omega_{i-1}^{+} \\ \Omega_{i-1}^{-} \end{pmatrix}, \quad \text{(A5)}$$

where $a_{11}=\frac{1}{2}(S_a^{-1}S_0+T_a^{-1}T_0)$, $a_{12}=\frac{1}{2}(S_a^{-1}S_0-T_a^{-1}T_0)$, and $a_{21}=a_{12}$, $a_{22}=a_{11}$.

The slice S matrix can be directly obtained from Eq. (A5),

$$s^i=\begin{pmatrix} s_{11}^i & s_{12}^i \\ s_{21}^i & s_{22}^i \end{pmatrix}=\begin{pmatrix} p_1t_1+p_2t_2 & p_1t_2+p_2t_1 \\ p_1t_2+p_2t_1 & p_1t_1+p_2t_2 \end{pmatrix}, \quad \text{(A6)}$$

where $p_1=[a_{11}-e^{i\beta h}a_{12}a_{11}^{-1}e^{i\beta h}a_{12}]^{-1}$, $p_2=a_{11}^{-1}e^{i\beta h}a_{12}[a_{11}-e^{i\beta h}a_{12}a_{11}^{-1}e^{i\beta h}a_{12}]^{-1}$, $t_1=e^{i\beta h}a_{11}$, and $t_2=-a_{12}$.

The overall S matrix of the whole unit cell is connected to individual slice S matrix through a recursion algorithm. Suppose the overall S matrix for the first $n-1$ slices and the S matrix for slice n have been calculated to be S^{n-1} and s^n, respectively, the overall S matrix for the first n slices S^n is given by[23,24,33]

$$S_{11}^n=s_{11}^n[I-S_{12}^{n-1}s_{21}^n]^{-1}S_{11}^{n-1}, \quad \text{(A7)}$$

$$S_{12}^n=s_{12}^n+s_{11}^nS_{12}^{n-1}[I-s_{21}^nS_{12}^{n-1}]^{-1}s_{22}^n, \quad \text{(A8)}$$

$$S_{21}^n=S_{21}^{n-1}+S_{22}^{n-1}s_{21}^n[I-S_{12}^{n-1}s_{21}^n]^{-1}S_{11}^{n-1}, \quad \text{(A9)}$$

$$S_{22}^n=S_{22}^{n-1}[I-s_{21}^nS_{12}^{n-1}]^{-1}s_{22}^n, \quad \text{(A10)}$$

where I is a unit matrix. We note here there is a type error in Eq. (8b) of Ref. 33.

The above procedure of S-matrix construction is for a general photonic structure without considering any possible structural symmetry. In the presence of mirror-reflection symmetries, the construction of the S matrix essentially follows the same procedure from Eqs. (A1)–(A6), except that the matrices S_a, T_a, S_0, and T_0 will take the suitable form in the corresponding symmetry-reduced irreducible plane-wave space. At the same time, the column vectors $\Omega_{i-1}^{\pm}$ and $\Omega_i^{\pm}$ should only contain those corresponding truly independent plane-wave coefficients in the air films, as has been shown in Eqs. (3.36)–(3.43). We notice here that the recursion algorithm (A7)–(A10) keeps the same in all symmetry situations.

APPENDIX B: SOLUTION OF PHOTONIC BAND STRUCTURES FROM THE UNIT-CELL *S* MATRIX

The S matrix for the unit cell of a photonic crystal S is defined as

$$\begin{pmatrix} \Omega_1^{+} \\ \Omega_0^{-} \end{pmatrix}=S\begin{pmatrix} \Omega_0^{+} \\ \Omega_1^{-} \end{pmatrix}=\begin{pmatrix} S_{11} & S_{12} \\ S_{21} & S_{22} \end{pmatrix}\begin{pmatrix} \Omega_0^{+} \\ \Omega_1^{-} \end{pmatrix}, \quad \text{(B1)}$$

where $\Omega_1^{\pm}$ and $\Omega_0^{\pm}$ are the plane-wave coefficient column vectors in the right- and left-hand sides of the unit cell, and S_{ij} $(i,j=1,2)$ are four block submatrices of S. Using the relation satisfied by an eigenmode as

$$\begin{pmatrix} \Omega_1^{+} \\ \Omega_1^{-} \end{pmatrix}=\lambda\begin{pmatrix} \Omega_0^{+} \\ \Omega_0^{-} \end{pmatrix}, \quad \text{(B2)}$$

the eigenproblem can be cast into the following form:

$$\begin{pmatrix} S_{11} & 0 \\ S_{21} & -I \end{pmatrix}\begin{pmatrix} \Omega_0^{+} \\ \Omega_0^{-} \end{pmatrix}=\lambda\begin{pmatrix} I & -S_{12} \\ 0 & -S_{22} \end{pmatrix}\begin{pmatrix} \Omega_0^{+} \\ \Omega_0^{-} \end{pmatrix}. \quad \text{(B3)}$$

Equation (B3) is a standard form of generalized eigenproblem $Ax=\lambda Bx$, where A and B are both square matrices, λ is the eigenvalue, and x is the eigenvector. So we can use some standard eigensolution algorithms to solve the eigenvalues and eigenvectors of Eq. (B3). For a Bloch's mode, we set $\lambda=e^{i\mathbf{k}\cdot\mathbf{R}}$, where $\mathbf{k}$ is the Bloch wave vector, and $\mathbf{R}$ is the primitive lattice vector. This leads to the dispersions (band structures) of the photonic crystal. In the case of a lossy mode, e.g., in a lossy photonic crystal waveguide, the eigenvalue can be cast as $\lambda=e^{ikh-\beta h}$, where k is the wave vector, β is the decay constant, and h is the lattice spacing along the waveguide axis.

In the case of adoption of a large plane-wave number, e.g. in order to guarantee a good numerical accuracy, there will exist eigenvalues whose modulus are extremely large. These correspond to strongly evanescent waves. In this situation, a more reliable way to find the dispersion is not to directly solve λ as in Eq. (B3), but to solve $(\lambda+1)^{-1}$, which do not cause overflow or underflow for $|\lambda|\gg 1$ or $|\lambda|\ll 1$. From the equality $Ax=\lambda Bx$, we can derive $Bx=(\lambda+1)^{-1}(A+B)x$, or equivalently from Eq. (B2) we can find

$$\begin{pmatrix} I & -S_{12} \\ 0 & -S_{22} \end{pmatrix}\begin{pmatrix} \Omega_0^{+} \\ \Omega_0^{-} \end{pmatrix}=(\lambda+1)^{-1}\begin{pmatrix} I+S_{11} & -S_{12} \\ S_{21} & -I-S_{22} \end{pmatrix}\begin{pmatrix} \Omega_0^{+} \\ \Omega_0^{-} \end{pmatrix}. \quad \text{(B4)}$$

We note here the solution of dispersion through the S matrix follows the same procedure irrespective of the structural symmetry. All symmetry information has been involved in the S matrix itself.

*Email address: lizy@axel.ameslab.gov

[1] E. Yablonovitch, Phys. Rev. Lett. **58**, 2059 (1987).
[2] J.D. Joannopoulos, R.D. Meade, and J.N. Winn, *Photonic Crystals* (Princeton University Press, Princeton, NJ, 1995).
[3] A. Mekis, J.C. Chen, I. Kurland, S. Fan, P.R. Villeneuve, and J.D. Joannopoulos, Phys. Rev. Lett. **77**, 3787 (1996).
[4] S.Y. Lin, E. Chow, V. Hietala, P.R. Villeneuve, and J.D. Joannopoulos, Science **282**, 274 (1998).
[5] K.M. Ho, C.T. Chan, C.M. Soukoulis, R. Biswas, and M. Sigalas, Solid State Commun. **89**, 413 (1994).
[6] S.Y. Lin, J.G. Fleming, D.L. Hetherington, B.K. Smith, R. Biswas, K.M. Ho, M.M. Sigalas, W. Zurbrzycki, S.R. Kurtz, and J. Bur, Nature (London) **394**, 251 (1998).
[7] J.G. Fleming and S.Y. Lin, Opt. Lett. **24**, 49 (1999).
[8] S. Noda, K. Tomoda, N. Yamamoto, and A. Chutinan, Science **289**, 604 (2000).
[9] A. Chutina and S. Noda, Appl. Phys. Lett. **75**, 3739 (1999).
[10] M. Bayindir, E. Ozbay, B. Temelkuran, M.M. Sigalas, C.M. Soukoulis, R. Biswas, and K.M. Ho, Phys. Rev. B **63**, 081107 (2001).
[11] Z.Y. Li and K.M. Ho, J. Opt. Soc. Am. B **20**, 801 (2003).
[12] C. Sell, C. Christensen, G. Tuttle, Z.Y. Li, and K.M. Ho (unpublished).
[13] S.G. Johnson, S. Fan, P.R. Villeneuve, J.D. Joannopoulos, and L.A. Kolodziejski, Phys. Rev. B **60**, 5751 (1999).
[14] A. Chutina and S. Noda, Phys. Rev. B **62**, 4488 (2000); A. Chutinan, M. Mochizuki, M. Imada, and S. Noda, Appl. Phys. Lett. **79**, 2690 (2001).
[15] M. Tokushima, H. Kosaka, A. Tomita, and H. Yamada, Appl. Phys. Lett. **76**, 952 (2000).
[16] E. Chow, S.Y. Lin, S.G. Johnson, P.R. Villineneve, J.D. Joannopoulos, J.R. Wendt, G.A. Vawter, W. Zubrzycki, H. Haus, and A. Allenman, Nature (London) **407**, 983 (2000).
[17] M. Loncar, D. Nedeljkovic, T. Doll, J. Vuckovic, A. Scherer, and T.P. Pearsall, Appl. Phys. Lett. **77**, 1937 (2000).
[18] C.J.M. Smith, H. Benisty, S. Olivier, M. Rattier, C. Weisbuch, T.F. Krauss, R.M. De La Rue, R. Houdre, and U. Oesterle, Appl. Phys. Lett. **77**, 2813 (2000).
[19] K.M. Ho, C.T. Chan, and C.M. Soukoulis, Phys. Rev. Lett. **65**, 3152 (1990).
[20] Z.Y. Li, J. Wang, and B.Y. Gu, Phys. Rev. B **58**, 3721 (1998).
[21] S.G. Johnson and J.D. Joannopoulos, Opt. Express **8**, 173 (2001).
[22] A. Taflove and S.C. Hagness, *Computational Electrodynamics: The Finite-Difference Time-Domain Method* (Artech House, Boston, 2000).
[23] J.B. Pendry, J. Mod. Opt. **41**, 209 (1994).
[24] L. Li, J. Opt. Soc. Am. A **13**, 1024 (1996).
[25] L. Li, J. Opt. Soc. Am. A **14**, 2758 (1997).
[26] E. Silberstein, P. Lalanne, J.P. Hugonin, and Q. Cao, J. Opt. Soc. Am. A **18**, 2865 (2001).
[27] Z.Y. Li and K.M. Ho, Phys. Rev. B **67**, 165104 (2003).
[28] Z.Y. Li and L.L. Lin, Phys. Rev. E **67**, 046607 (2003).
[29] I.R. Matias, I. Del Villar, F.J. Arregui, and R.O. Claus, J. Opt. Soc. Am. A **20**, 644 (2003).
[30] Z. Y. Li and K. M. Ho, Phys. Rev. B **68**, 155101 (2003).
[31] E. Noponen and J. Turunen, J. Opt. Soc. Am. A **11**, 2494 (1994).
[32] P. Dansas and N. Paraire, J. Opt. Soc. Am. A **15**, 1586 (1998).
[33] L.L. Lin, Z.Y. Li, and K.M. Ho, J. Appl. Phys. **94**, 811 (2003).
[34] A. Adibi, Y. Xu, R.K. Lee, A. Yariv, and A. Scherer, Phys. Rev. B **64**, 033308 (2001).
[35] E. Miyai, M. Okano, M. Mochizuki, and S. Noda, Appl. Phys. Lett. **81**, 3729 (2002).
[36] J.P. Berenger, J. Comput. Phys. **114**, 185 (1994).
[37] S. Noda, A. Chutinan, and M. Imada, Nature (London) **407**, 608 (2000).